

STAR FORMATION RELATIONS IN THE MILKY WAY

NALIN VUTISALCHAVAKUL¹, NEAL J. EVANS II¹, MARK HEYER²

¹Department of Astronomy, The University of Texas at Austin, 2515 Speedway, Stop C1400, Austin, Texas 78712-1205, U.S.A.

²Department of Astronomy, University of Massachusetts, Amherst, Massachusetts 01003, U. S. A.

ABSTRACT

The relations between star formation and properties of molecular clouds are studied based on a sample of star forming regions in the Galactic Plane. Sources were selected by having radio recombination lines to provide identification of associated molecular clouds and dense clumps. Radio continuum and mid-infrared emission were used to determine star formation rates, while ¹³CO and submillimeter dust continuum emission were used to obtain masses of molecular and dense gas, respectively. We test whether total molecular gas or dense gas provides the best predictor of star formation rate. We also test two specific theoretical models, one relying on the molecular mass divided by the free-fall time, the other using the free-fall time divided by the crossing time. Neither is supported by the data. The data are also compared to those from nearby star forming regions and extragalactic data. The star formation “efficiency,” defined as star formation rate divided by mass, spreads over a large range when the mass refers to molecular gas; the standard deviation of the log of the efficiency decreases by a factor of three when the mass of relatively dense molecular gas is used rather than the mass of all the molecular gas.

Keywords: stars: formation

1. INTRODUCTION

Given the importance of star formation in the evolution of galaxies, understanding the regulation of star formation is crucial. Early work on star formation on galaxy scales relied on empirical star formation laws (Schmidt 1959; Kennicutt 1989), with little connection to the detailed studies of star formation in our own Galaxy. Recently there has been more focus on integrating the understanding of the process of star formation from the scale of galaxies to the much smaller scales of regions within molecular clouds (Kennicutt & Evans 2012; Kruijssen & Longmore 2014; Krumholz 2014).

While large scale studies provide essential information on the relation between large scale properties of galaxies and star formation, the process of converting gas into stars takes place on a smaller scale. Since molecular clouds (MCs) are the sites of star formation in galaxies, it is essential to establish the key processes and sequences within molecular clouds that regulate the production of newborn stars in order to gain a deeper understanding of processes at galactic scales. While there are some recent high-spatial resolution studies of nearby galaxies that can resolve regions of MCs (e.g., Rosolowsky et al. 2007; Hughes et al. 2013), the Milky Way offers the highest resolution view to investigate the connection between star formation and the local gas properties.

There are several recent surveys of dust and molecular line emission in the Milky Way that provide information on the distributions and properties of MCs. Ideally, star formation in MCs can be directly evaluated by identifying stars or young-stellar objects inside the clouds, which along with the information on their mass and lifetime provide a good estimate of star formation rate (SFR) for the clouds. This direct method of estimating SFR has been applied for nearby ($d < 830$ pc) molecular clouds (Heiderman et al. 2010; Gutermuth et al. 2011; Lada et al. 2010; Evans et al. 2014), but these have a limited range in properties, making it difficult to test theories for the importance of cloud properties in controlling star formation rates. Furthermore, they are primarily low-mass ($\langle M_{\text{cloud}} \rangle \sim 3000 M_{\odot}$) clouds (Heiderman et al. 2010) whose star formation does not fully sample the IMF. Their star formation activity would be almost entirely invisible to observers in other galaxies. The goal of this paper is to extend this effort to larger clouds where massive stars are formed, both to sample a larger range of cloud properties and to examine regions more comparable to those that can be observed in other galaxies.

The challenge is that the more massive clouds with more fully sampled IMFs are all quite distant; even Orion does not sufficiently sample the IMF to use the extragalactic indicators of star formation rate (Kennicutt & Evans 2012). For those distant clouds, counting YSOs is very difficult, both because of sensitivity limits and because of background source confusion (Dunham et al. 2011), although recent work has been more successful (Heyer et al. 2016). To study star formation in a larger sample of Galactic MCs, we resort to indirect tracers of SFR, such as those commonly used in extragalactic studies including $H\alpha$, UV continuum, total infrared luminosity, mid-infrared emission, and radio continuum emission. The shorter wavelength tracers ($H\alpha$, UV continuum) cannot be used in the plane of the Galaxy because of dust obscuration, and the total far-infrared luminosity awaits full release of surveys with *Herschel*. In this study, we use mid-infrared and radio continuum emission. It is known that these indirect tracers derived from extragalactic data are problematic when applied to smaller regions such as MCs. The problem arises mostly from the assumptions of a fully-sampled IMF and a star formation history that is constant over a long timescale (Kruijssen & Longmore 2014; Krumholz et al. 2015). Several recent studies of SFR tracers in regions with different properties suggest that some tracers offer reasonable measures of SFR (although still with large scatter) in regions above a certain minimum SFR (Wu et al. 2005; Vutisalchavakul & Evans 2013).

In this paper, we collect data from surveys of radio recombination lines, radio continuum, and mid-infrared emission to measure SFR, ^{13}CO spectroscopy to evaluate MC properties, and millimeter dust continuum emission to trace the dense gas component. We describe these data sets in §2 and summarize our selection of star forming regions and their association with gas in §3. Various models for star formation prediction are tested with these data in §5. In §6, we compare our results to similar studies of nearby clouds, and in §7, we put our results into the context of studies of other galaxies.

2. DATA

2.1. Radio Recombination Lines and H II Region Catalog

Anderson et al. (2014), hereafter A14, compiled a catalog of H II regions within the Milky Way. The A14 catalog comprises over 8000 Galactic H II regions and H II region candidates identified by mid-infrared (MIR) emission morphology using WISE 12 μm and 22 μm data. Many of these sources are associated with radio recombination lines (hereafter RRLs) $H86\alpha$ through $H96\alpha$ (Anderson et al. 2011) or $H\alpha$ emission, confirming their association with H II regions.

2.2. Radio Continuum Data

Radio continuum emission closely associated with recent star formation in the Milky Way comes from free-free emission of ionized gas around high-mass stars. The Very Large Array Galactic Plane Survey (VGPS), observed the H I spectral line and 21 cm radio continuum emission from the first Galactic quadrant covering the Galactic longitude between $18^\circ < l < 67^\circ$ with varying Galactic latitude range from $|b| < 1.3^\circ$ to 2.3° at the resolution of $1'$ (Stil et al. 2006). To provide sensitivity on larger scales, short spacing data obtained with the Green Bank Telescope were added to the interferometric continuum data.

2.3. Mid-Infrared Data

The Wide-field Infrared Survey Explorer (WISE) mapped the entire sky in four IR bands at 3.4, 4.6, 12, and 22 μm (Wright et al. 2010). The MIR band at 22 μm , which has a resolution of $12''$, provides a measure of star formation rate. The WISE Image Atlas provides image tiles covering $1.564^\circ \times 1.564^\circ$ in area with $1.375''$ per pixel. Larger 22 μm image mosaics covering the segment of the Galactic Plane in this study were generated from the set of image tiles using the MONTAGE mosaic software (Jacob et al. 2010). The characteristic saturation level for the point sources, defined to be the level at which 50% of the sources have some saturated pixels, in the 22 μm band is about 12 Jy. For a few bright sources that are saturated in the WISE 22 μm band, we use the data from the Infrared Astronomical Satellite (IRAS) 25 μm band. The IRAS Improved Reprocessing of the IRAS Survey (IRIS) provides images of the sky at 25 μm band at the resolution of $\approx 4'$ (Miville-Deschênes & Lagache 2005). The resolution of IRAS 25 μm data is considerably lower than that of WISE 22 μm band; therefore, we use IRAS 25 μm images for sources saturated in WISE 22 μm only if the source is resolved with no confusion with other nearby sources.

2.4. $^{13}\text{CO } J = 1 \rightarrow 0$ Emission

Data from the Boston University-FCRAO Galactic Ring Survey (GRS) and the Exeter-FCRAO Galactic Plane Survey (EXFC) provide data on molecular clouds. The GRS surveyed the $^{13}\text{CO } J = 1 \rightarrow 0$ emission between Galactic

longitudes $18^\circ < l < 55.7^\circ$ and Galactic latitudes, $|b| < 1^\circ$ using the Five College Radio Astronomy Observatory 14-m telescope (Jackson et al. 2006). The LSR velocity (v_{LSR}) coverage is from -5 to 135 km s^{-1} for $l \leq 40^\circ$ and from -5 to 85 km s^{-1} for $l > 40^\circ$. The final data cubes are gridded at $22''$ and at velocity resolution of 0.21 km s^{-1} . The median main beam sensitivity of the GRS is 0.21 K . The EXFC survey covered ^{12}CO and $^{13}\text{CO } J = 1 \rightarrow 0$ emission within two areas: $55.7^\circ < l < 102.5^\circ$, $|b| < 1^\circ$ and $141^\circ < l < 192^\circ$, $-3.5^\circ < b < 5.5^\circ$ with the FCRAO 14 m telescope (Roman-Duval et al. 2016). The median main beam sensitivity at 110 GHz in the area of this study is 0.46 K . For both the GRS and EXFC surveys, the half power beam width of the telescope at 110 GHz is $48''$. All of the ^{13}CO data used in this study (GRS and EXFC) have been post-processed to remove contributions from the antenna error beam.

2.5. Millimeter Dust Continuum Emission

The dense gas within molecular clouds is examined using 1.1 mm dust emission from the Bolocam Galactic Plane Survey (BGPS). The BGPS observed part of the Galactic Plane at the effective resolution of $33''$ and 1σ sensitivity ranging from 30 to 100 mJy per beam (Aguirre et al. 2011; Ginsburg et al. 2013). The BGPS provides contiguous observational data over the ranges of $|b| < 0.5^\circ$ for $-10.5^\circ < l < 90.5^\circ$, $|b| < 1.5^\circ$ for $75.5^\circ < l < 87.5^\circ$, and additional coverages over selected regions described in Aguirre et al. (2011) and Ginsburg et al. (2013).

Owing to the removal of atmospheric signal by spatial filtering, the data from BGPS recovers most of the astrophysical emission out to the scale of $80''$ and partially recovers emission out to the scale of $300''$ (Ginsburg et al. 2013). The spatial filtering subtracts signal from molecular clouds that subtend solid angles greater than $300''$. For these reasons, the data are sensitive to compact regions within clouds with enhanced column densities, and likely, volume densities.

The BGPS version 2.1 data release includes a source catalog extracted from 1.1 mm maps using a seeded watershed algorithm (Rosolowsky et al. 2010; Ginsburg et al. 2013). The Bolocat V2.1 consists of 8594 sources with 1.1 mm flux from photometry (background-subtracted) for the aperture radii of $20''$, $40''$, and $60''$, as well as flux integrated over the source area.

All the Bolocat sources in version 1 of the BGPS catalog within the Galactic longitude range of $7.5^\circ < l < 194^\circ$ were followed up with spectroscopic observations of dense gas tracers, using the HCO^+ and N_2H^+ 3-2 transitions with the Arizona Radio Observatory Submillimeter Telescope (Schlingman et al. 2011; Shirley et al. 2013) with 51% of the sources detected in at least one of the molecular lines. Additional molecular line observations of NH_3 (1,1), (2,2), and (3,3) inversion lines are available for sources in the inner Galaxy from the Green Bank Telescope (Dunham et al. 2011). The molecular line observations of the Bolocat sources provide kinematic information to link the dust continuum source to its parent molecular cloud and the H II regions.

3. ANALYSIS

In this section we describe the selection criteria for the sample of star forming regions (§3.1), the calculations of star formation rates (§3.2), and the extraction and measurement of the properties of MCs and dense gas (§3.3).

3.1. The Samples

Studies of star formation in the plane of the Galaxy are challenging because it is non-trivial to clearly associate a star forming event, identified by broad-band photometry, with a particular molecular cloud. In this study, the detection of a hydrogen radio recombination line (RRL) arising within an H II region is required as a marker of star formation because we need velocity information to tie the star formation to the molecular gas. Target sources with well defined distances are selected from the compilation of H II regions with a RRL by A14. First, we restrict our source list to Galactic longitudes, $30^\circ < l < 63^\circ$ to sample a volume of the disk that is external to the stellar bar but crosses the Scutum and Sagittarius spiral arms and extends to the Vulpecula Rift. To ensure coverage by the GRS, whose minimum velocity is -5 km s^{-1} , the LSR velocities of the radio recombination lines (v_{RRL}) are restricted to be greater than 0 km s^{-1} . A consequence of excluding negative velocities in this longitude range is the exclusion of star forming regions on the far side of the Galaxy with Galactic radii greater than 8.5 kpc. The primary sample of 66 sources comprises the RRLs that could be associated with MCs. The positions, velocities, and distances of the selected sample are listed in Table 1. The sample size is reduced to 51 sources after a minimum star formation rate is imposed (§3.2.3).

When testing relations between dense gas and star formation properties, we further restricted the sample to sources that can be linked to one or more sources from the BGPS survey of 1.1 mm dust continuum emission sources (Ginsburg et al. 2013) and follow-up spectral line observations in HCO^+ and N_2H^+ (Schlingman et al. 2011; Shirley et al. 2013). To augment the sample, we include a subset of BGPS sources studied by Battisti & Heyer (2014) that are also associated with RRL H II regions. The resulting sample size for dense gas relations is 44.

Table 1. Radio Recombination Line Sources

WISE Name	l (deg)	b	v_{RRL} (km s ⁻¹)	D (kpc)	$\sigma(D)$	R_{GAL} (kpc)	Ref. ^a
G031.561+00.376	31.561	0.377	24.3	13.0	0.4	6.9	2,2
G032.077-00.230	32.077	-0.229	97.7	8.2	1.4	4.7	2,2
G032.030+00.048	32.030	0.049	91.1	7.2	1.2	4.8	1,1
G032.272-00.226	32.272	-0.226	21.5	12.8	0.7	7.1	1,1
G032.473+00.204	32.473	0.204	47.0	11.2	1.7	6.1	1,1
G032.582+00.001	32.590	-0.001	77.4	9.4	1.8	5.2	1,1
G032.587-00.330	32.587	-0.330	103.8	7.2	1.3	4.6	1,1
G032.733+00.209	32.733	0.209	16.1	13.2	1.4	7.3	1,1
G032.870-00.427	32.870	-0.427	50.6	10.9	1.7	6.0	1,1
G033.419-00.005	33.419	-0.004	76.5	9.3	1.8	5.3	1,1
G033.643-00.229	33.643	-0.228	102.9	7.1	1.1	4.7	1,1
G033.809-00.190	33.809	-0.190	40.3	11.4	0.9	6.4	1,1
G033.941-00.039	33.942	-0.039	57.2	10.4	1.1	5.8	1,1
G034.041+00.052	34.041	0.053	36.4	11.6	0.7	6.5	1,1
G034.089+00.438	34.089	0.438	32.6	11.8	1.3	6.7	1,1

^a First and second number cites the reference for the v_{RRL} and distance values respectively. 1:(Anderson et al. 2014), 2:(Battisti & Heyer 2014), 3:(Ellsworth-Bowers et al. 2015)

NOTE—Table 1 is published in its entirety in the electronic edition of the *Astrophysical Journal*. A portion is shown here for guidance regarding its form and content.

The choice of requiring H II regions means that all the star-forming regions associated with molecular clouds in this study are forming high-mass stars, making the use of infrared and radio continuum tracers less problematic. The sample is clearly biased against starless clouds or even clouds with low-level star formation similar to that in solar-neighborhood clouds.

3.1.1. Assigning Distances

Distances to most of the target RRL regions are derived by A14 using trigonometric parallax of associated masers or more typically, kinematic distances assuming the rotation curve of the Milky Way derived by Brand & Blitz (1993) and resolving the distance ambiguity for the inner Galaxy. For 9 sources where distances for the RRL H II regions are not defined by A14, the cloud distance is assigned to the mean of the distances from the associated Bolocat sources, where distances were obtained from Ellsworth-Bowers et al. (2015), who adopted the rotation curve of Reid et al. (2009). For the 9 sources taken from Battisti & Heyer (2014), we adopt the distance used in their study that assumed the rotation curve of Clemens (1985). The difference in distances using the three rotation curves is small compared to other uncertainties with the kinematic distance method. The mean fractional distance uncertainties, $\sigma(D)/D$, for objects in our sample are 0.15 for A14, 0.19 for Ellsworth-Bowers et al. (2015), and 0.20 for Battisti & Heyer (2014). The molecular clouds are assigned distances of the H II regions with which these are associated. For sources without a spectroscopic dense gas tracer, velocities were obtained by connecting molecular gas observations from the GRS ¹³CO data to Bolocat sources (Ellsworth-Bowers et al. 2015). The combination of dense gas tracers and ¹³CO data resulted in 45% of the Bolocat V2.1 sources with assigned v_{LSR} . The distance uncertainties are estimated from the combined uncertainties in the choice of Galactic rotation curve, the streaming motions of 7 km s⁻¹, and the solar circular rotation speed (Anderson et al. 2012, 2014).

The sources span a large range of heliocentric distances of 1.7 to 13.2 kpc, with an average distance of 8 ± 3 kpc and a median of 8.1 kpc. The span of Galactocentric radii (R_{GAL}) is less, ranging from 4.6 to 8 kpc with an average of 6.3 ± 0.8 kpc and a median of 6.1 kpc. They should be more representative of star formation activity in the Galaxy than nearby, well-studied targets such as those in the Gould Belt (Dunham et al. 2015).

3.2. Star Formation Rates

Table 2. Star Formation Rates

WISE Name	SFR _{radio} (M _⊙ /Myr)	σ(SFR _{radio}) (M _⊙ /Myr)	SFR _{MIR} (M _⊙ /Myr)	σ(SFR _{MIR}) (M _⊙ /Myr)
G031.561+00.376	120.30	12.03	31.01	3.10
G032.077-00.230	58.60	5.86	150.80	15.08
G032.030+00.048	45.18	4.52	119.79	11.98
G032.272-00.226	39.06	3.91	34.12	3.41
G032.473+00.204	9.94	0.99	24.05	2.41
G032.582+00.001	11.64	1.16	6.98	0.70
G032.587-00.330	12.60	1.26	10.71	1.07
G032.733+00.209	148.94	14.89	176.60	17.66
G032.870-00.427	35.57	3.56	49.42	4.94
G033.419-00.005	45.24	4.52	63.96	6.40
G033.643-00.229	6.86	0.69	0.00	0.00
G033.809-00.190	30.38	3.04	82.71	8.27
G033.941-00.039	89.57	8.96	41.53	4.15
G034.041+00.052	28.04	2.80	206.83	20.68
G034.089+00.438	24.02	2.40	40.01	4.00

NOTE—Table 2 is published in its entirety in the electronic edition of the *Astrophysical Journal*. A portion is shown here for guidance regarding its form and content.

The radio continuum at 21 cm and MIR emission at 22 or 25 μm are the star formation tracers used in this study. We refer to them as “radio” and “MIR” in what follows. Using continuum emission as a tracer creates a problem of source confusion between different emitting regions along the line of sight. If more than one emitting region lies within the angular vicinity of a MC, one cannot distinguish which regions are associated with the MC. To mitigate the problem of confusion along the line of sight, the RRL data are used to associate radio continuum emission and MIR emission with molecular gas by requiring velocity agreement with the molecular gas (see §3.2.1).

3.2.1. Star Formation Rates Derived from Radio Continuum Emission

For each of the RRL locations, a region of associated radio continuum emission is defined using the following steps. First, the radio emission is fitted to a 2D-Gaussian profile, centered on the RRL position. If the emission is reasonably well fitted with the 2D-Gaussian, the source is labeled as a compact source with sizes (σ_x, σ_y) of the fitted Gaussian. The radio flux is calculated from aperture photometry with an aperture radius $3(\sigma_x + \sigma_y)/2$ and an appropriate sky annulus. If the radio emission could not be fitted well with a 2D Gaussian (which is the case if the source is extended or in a crowded region), then a polygon is used to define the region of the source emission and another region for estimating background emission. The RRL sources with no significant radio continuum emission above the background are excluded from further analysis.

If more than one RRL source is found within the solid angle of the radio aperture and RRL velocities are within ± 5 km s⁻¹ of each other, then the RRL sources are considered as a single star-forming region. If the velocities differ by more than 5 km s⁻¹ and the radio emission cannot be separated, then the sources are excluded from our target list.

Radio emission from galaxies is comprised of both synchrotron and free-free emission components with synchrotron emission dominating at 21 cm (Condon 1992). In contrast, the higher spatial resolution in the Milky Way surveys favors localized regions of free-free emission. Since our targets are selected by the detection of the hydrogen recombination line, we assume the origin of the 21 cm signal is free-free emission from an H II region excited by ionizing far-UV radiation from massive stars. Therefore, we do not use the extragalactic relation between radio emission and star formation, which is primarily a relation between synchrotron emission on large scales and star formation averaged over about 100 Myr (Kennicutt & Evans 2012). Instead, we use the compact free-free radiation from the H II region, which, like H α , averages over about 3 Myr (Hao et al. 2011; Kennicutt & Evans 2012).

The free-free emission is related to the ionizing luminosity by the expression

$$\frac{N_{\text{UV}}}{\text{phot s}^{-1}} = 6.3 \times 10^{52} \left(\frac{T_e}{10^4 \text{K}} \right)^{-0.45} \left(\frac{\nu}{\text{GHz}} \right)^{0.1} \times \left(\frac{L_{\text{T}}}{10^{20} \text{W Hz}^{-1}} \right), \quad (1)$$

where N_{UV} is the number of Lyman continuum photons per second, T_e is the electron temperature, ν is the frequency, and L_{T} is the thermal emission luminosity assuming optically thin gas (Condon 1992). For an electron temperature of 10^4 K, and an IMF described by (Chomiuk & Povich 2011), the SFR is calculated from

$$\text{SFR}(\text{radio}) = 0.47 \times 10^{-14} \left(\frac{\nu}{\text{GHz}} \right)^{0.1} \times \left(\frac{L_{\text{T}}}{\text{W Hz}^{-1}} \right) M_{\odot} \text{Myr}^{-1} \quad (2)$$

(Chomiuk & Povich 2011; Vutisalchavakul & Evans 2013).

This expression may underestimate the SFR if UV photons are not absorbed, as in the case of a density bounded H II region. If a Salpeter slope is continued down to $0.1 M_{\odot}$, the derived SFRs would be 1.44 times higher (Chomiuk & Povich 2011). The star formation rates derived from radio emission for our sample of RRL regions are listed in Table 2.

3.2.2. Star Formation Rates Derived from MIR Emission

The process used to define the MIR-emitting region associated with a RRL source is similar to the method used for radio continuum images described in the previous section. The MIR emission at the location of the radio continuum region is examined. If the distribution of MIR emission is compact and isolated, it is fitted to a 2D Gaussian profile. Otherwise we define the emitting region with a polygon. Photometry for all of the MIR emitting regions is performed similarly to the radio continuum regions. Most of the sources that are compact in radio images are also compact in MIR emission. In the case of G033.643-00.229, the background subtracted flux is less than zero. This target is excluded from subsequent analyses.

The SFR is calculated from the extragalactic relation (Calzetti et al. 2007):

$$\text{SFR}(\text{MIR}) = 1.27 \times 10^{-32} \times [L_{24}(\text{ergs s}^{-1})]^{0.885} (M_{\odot} \text{Myr}^{-1}) \quad (3)$$

where L_{24} is the $24\mu\text{m}$ luminosity. The IMF assumed by Calzetti et al. (2007) is consistent with that used for the SFR from the radio continuum emission. Here, we substituted the WISE 22 μm or the IRAS 25 μm luminosity for the 24 μm luminosity. The corresponding star formation rates derived from the mid-infrared luminosity are listed in Table 2.

3.2.3. Comparing SFR from radio continuum and MIR

The two different estimations of SFR are compared in Figure 1. Because the luminosities of both tracers are proportional to a flux times the square of the distance, the uncertainties are computed by propagating a nominal 10% uncertainty in the flux measurement and the distance uncertainty in Table 1 (see the Appendix for a description of error propagation). The distance uncertainty is usually, but not always, dominant. The SFRs from the two tracers are comparable, with the SFR from MIR usually being somewhat higher, especially at low SFRs. The black solid line in Figure 1 is a line of equality, while the blue solid line is a fit to the data, using χ^2 minimization with errors in both variables. The fit is

$$\log[\text{SFR}(\text{MIR})] = a + b \log[\text{SFR}(\text{radio})] \quad (4)$$

with $a = 0.38 \pm 0.04$ and $b = 0.85 \pm 0.02$. The slope is nearly identical to that found by analysis of a more limited sample, while the coefficient is a bit less, but within the uncertainties: ($a = 0.53 \pm 0.17$ and $b = 0.83 \pm 0.08$) (Vutisalchavakul & Evans 2013); that fit is shown as a red line in Figure 1.

The slightly sub-linear fits and the larger discrepancies at low SFR can result from the fact that the radio emission is more sensitive to the upper end of the IMF (as is also true for H α or any diagnostic requiring ionized gas), as can be seen from Table 1 of Kennicutt & Evans (2012). For this reason, we use SFR(MIR) in further analysis. This tracer also begins to underestimate the SFR for SFRs less than about $5 M_{\odot} \text{Myr}^{-1}$, corresponding to a total far-infrared luminosity of $10^{4.5} L_{\odot}$ (Vutisalchavakul & Evans 2013; Wu et al. 2005). Consequently, we limit further investigation to those sources with SFR above this value, leaving 51 sources.

Even above the threshold of $5 M_{\odot} \text{Myr}^{-1}$, SFRs may be poorly estimated. The dominant source of uncertainty in SFR is the conversion from the star-formation tracers to SFR. The common method used to calculate the conversion factors is to use a stellar population synthesis model, stellar evolutionary models, and atmospheric models to connect

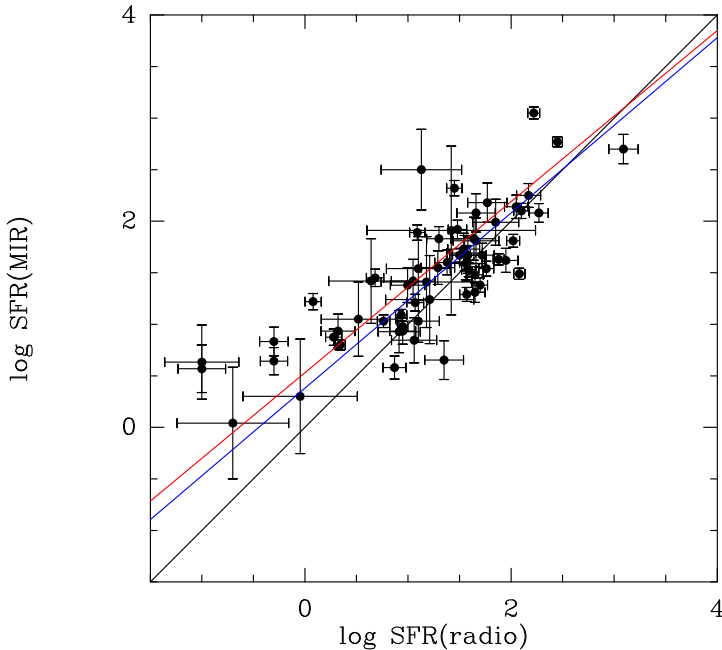


Figure 1. The comparison between SFR(MIR) and SFR(radio), measured in $M_{\odot} \text{ Myr}^{-1}$. The solid black line represents the 1-1 line where the two SFRs are equal. The blue line is a fit to the data, including uncertainties in both axes. The red line is fit to a smaller sample of sources from [Vutisalchavakul & Evans \(2013\)](#).

stellar populations to their photometric output. Then assumptions of a fully-sampled IMF and a star-formation history (SFH) connect the SFR of a region to the light output for each tracer ([Leitherer et al. 1999](#)). The effect of the stochastic sampling of the IMF and SFH on the reliability of the SFR tracers has been a topic of many recent studies ([Fumagalli et al. 2011](#); [da Silva et al. 2012, 2014](#); [Kruijssen & Longmore 2014](#); [Krumholz et al. 2015](#)). [da Silva et al. \(2014\)](#) used the Stochastically Lighting Up Galaxies (SLUG) simulations to study the effect of IMF and SFH sampling on the conversion from photometric observations of the star-formation tracers to SFR. Instead of a unique SFR for a given luminosity (in the tracers), the effect of IMF and SFH sampling results in probability distributions of SFR, which can have a large bias and scatter for regions with low SFR. The result from SLUG, given an input of a constant SFR on the timescale of 500 Myr, for the bolometric luminosity as a SFR tracer gives a scatter in the $\log(\text{SFR})$ of ≈ 0.6 dex in the SFR range of $10 - 100 M_{\odot} \text{ Myr}^{-1}$, assuming uncertainties in the flux of 0.25 dex ([da Silva et al. 2014](#)). Consistent with that analysis, the SFR(MIR) appears to underestimate SFR for the Milky Way by a factor of $\approx 2 - 3$ ([Chomiuk & Povich 2011](#)). Because the effect is usually to underestimate the SFR, we treat this as a systematic uncertainty, rather than including it in the individual SFRs.

3.3. Gas Structures

3.3.1. Molecular Cloud Properties

The linking of a molecular cloud to the radio recombination line H II regions is similar to the method employed by [Battisti & Heyer \(2014\)](#) to connect larger clouds to 1.1 mm continuum sources. A $100 \times 100 \text{ pc}^2 \times 40 \text{ km s}^{-1}$ data cube centered on the l, b, v_{RRL} coordinates of the H II region is extracted from the larger CO survey. For a handful of nearby sources, the 100 pc edge may lie outside the Galactic latitude boundary of the survey, in which case the area is truncated to the largest available square area. The segmentation program, CPROPS ([Rosolowsky & Leroy 2006](#)), is applied to these extracted data to identify sets (islands) of contiguous voxels with CO brightness temperatures above a given threshold value. This threshold is varied depending on the complexity of the local background emission generated by unrelated foreground and background molecular clouds with comparable radial velocities with the intent to determine the lowest threshold value that distinguishes a structure from this background emission. We do not examine substructure within these islands of emission.

For a given threshold, hundreds of structures may be identified by the segmentation algorithm distributed over the 10^4 pc^2 area and 40 km s^{-1} range. To narrow the search for the molecular cloud associated with the H II region, we select a subset of this list with the condition, $|v_{\text{CO}} - v_{\text{RRL}}| < 10 \text{ km s}^{-1}$, where v_{CO} is the velocity centroid of the CO structure. For each structure in this subset, the distribution of velocity-integrated CO emission and its spatial

relationship to the H II region are examined. A CO structure is assigned to the H II region if its boundaries enclose the H II region or if there is a local intensity maximum coincident with the H II region position. A structure may also be linked if the solid angle of the detected radio continuum emission from the H II region partially overlaps with the solid angle of the CO emitting region or if the respective boundaries of the radio continuum and CO emissions are within $2'$ (2 times the FWHM beam width of the radio continuum data) at some point along their perimeters. In several cases, no structure can be confidently assigned to the H II region position, so we select the structure with the most comparable velocity to the RRL velocity that is within 5 ^{13}CO FWHM beam widths of the H II region position. Two examples of the cloud extraction are shown in Figure 2.

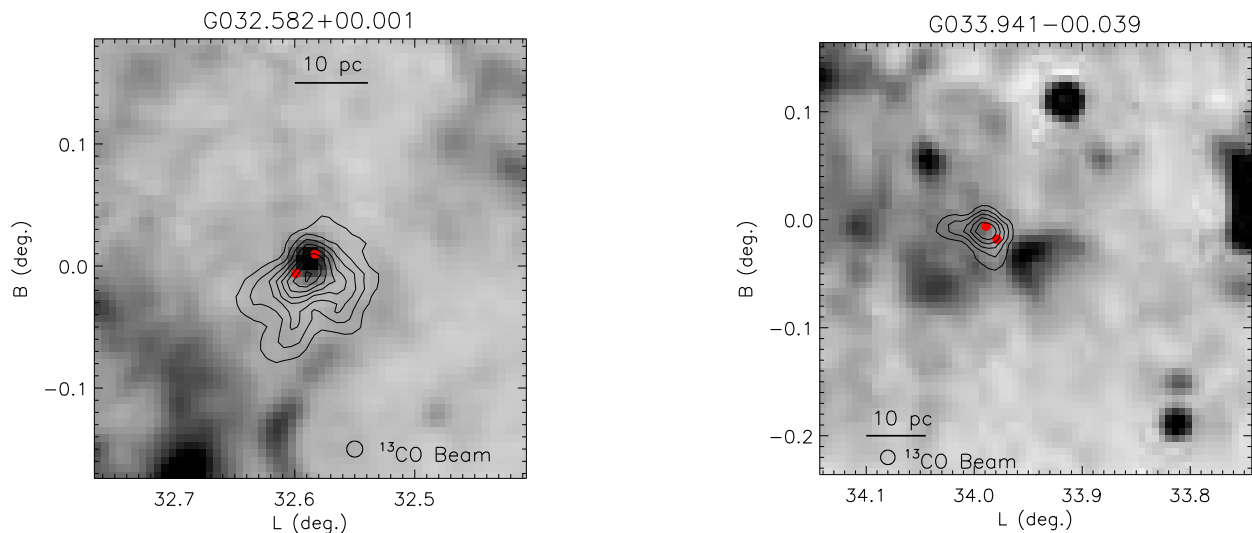


Figure 2. Images of integrated ^{13}CO $J = 1 \rightarrow 0$ emission (contours) overlaid on 21 cm continuum emission for RRL targets (left) G032.582+00.001 and (right) G033.941-00.039. Contours range from 1 to 15 K km s^{-1} spaced by 2 K km s^{-1} for G032.582+00.001 and 1 to 5 K km s^{-1} spaced by 1 K km s^{-1} for G033.941-00.039. The radio continuum source to the southwest of the cloud is the associated source. The solid, red circles mark the locations of associated Bolocam sources of dust continuum emission.

Once a cloud is linked to the H II region by the above criteria, its properties are determined from the set of voxels that comprise the structure. These properties include intensity-weighted positional moments and ^{13}CO luminosity. While the voxels that comprise the cloud are defined by the applied threshold, the cloud properties such as mass, size, and velocity dispersion, are extrapolated from this brightness temperature threshold to a hypothetical cloud edge at a brightness temperature of 0 K. The properties and uncertainties of each MC linked to an RRL source are summarized in Table 3.

For ^{13}CO data, column densities are derived following the expressions in Pineda et al. (2010). Here, we assume optically thin emission, so column density in the upper ($J = 1$) rotational energy level is

$$N_{1,\text{thin}} = \frac{8\pi k_B \nu_{10}^2}{hc^3 A_{10} C(T_{\text{ex}})} \int T_B(v) dv \quad (5)$$

where k_B is the Boltzmann constant, h is the Planck constant, c is the speed of light, and ν_{10} , A_{10} , T_B , T_{ex} are the frequency, Einstein A coefficient, brightness temperature, and excitation temperature for the ^{13}CO $J = 1 \rightarrow 0$ transition. The factor, $C(T_{\text{ex}})$, contains temperature dependent terms,

$$C(T_{\text{ex}}) = \left(1 - \frac{\exp(T_L/T_{\text{ex}}) - 1}{\exp(T_L/T_{\text{bg}}) - 1} \right) \quad (6)$$

Table 3. ^{13}CO Derived Molecular Properties

WISE Name	Type	r_{cloud}	$\sigma(r_{\text{cloud}})$	δv	$\sigma(\delta v)$	M_{cloud}	$\sigma(M_{\text{cloud}})$	M_{vir}	$\sigma(M_{\text{vir}})$	α	$\sigma(\alpha)$	n_{cloud}	$\sigma(n_{\text{cloud}})$	t_{ff}	$\sigma(t_{\text{ff}})$
		(pc)		(km s^{-1})		($10^3 M_{\odot}$)		($10^3 M_{\odot}$)				(cm^{-3})		(Myr)	
G031.561+00.376	2	15.81	8.57	1.30	0.23	66.3	26.8	31.1	20.1	0.47	0.36	60	105	4.1	7.1
G032.077-00.230	3	17.67	2.88	2.63	0.77	105.0	42.4	142.1	86.3	1.35	0.99	69	53	3.9	3.0
G032.030+00.048	2	27.21	0.01	1.88	0.01	180.6	72.9	111.8	1.2	0.62	0.25	32	19	5.6	3.3
G032.272-00.226	1	9.37	0.07	1.41	0.08	7.8	3.2	21.7	2.5	2.76	1.16	34	20	5.5	3.2
G032.473+00.204	1	15.56	0.05	2.06	0.03	101.7	41.1	76.8	2.2	0.75	0.31	97	57	3.2	1.9
G032.582+00.001	1	10.41	0.06	1.84	0.10	40.4	16.3	41.0	4.5	1.01	0.42	129	76	2.8	1.7
G032.587-00.330	1	10.06	0.02	2.28	0.03	20.7	8.3	60.8	1.6	2.94	1.19	73	43	3.7	2.2
G032.733+00.209	1	12.47	0.02	2.66	0.02	93.3	37.6	102.6	1.6	1.10	0.44	173	102	2.4	1.4
G032.870-00.427	1	13.56	0.02	1.59	0.03	72.5	29.3	39.8	1.5	0.55	0.22	105	62	3.1	1.8
G033.419-00.005	1	15.40	0.04	2.10	0.04	48.8	19.7	78.9	3.0	1.62	0.66	48	28	4.6	2.7
G033.643-00.229	3	24.88	0.01	2.85	0.01	232.3	93.8	234.9	1.7	1.01	0.41	54	32	4.3	2.6
G033.809-00.190	1	5.02	0.11	1.68	0.12	23.1	9.3	16.5	2.4	0.71	0.31	657	390	1.2	0.7
G033.941-00.039	2	8.63	0.23	1.75	0.23	21.4	8.7	30.7	8.1	1.43	0.69	120	72	2.9	1.7
G034.041+00.052	1	13.94	0.02	1.56	0.03	33.0	13.3	39.4	1.5	1.20	0.48	44	26	4.8	2.8
G034.089+00.438	1	7.39	0.04	1.47	0.04	12.2	4.9	18.6	1.0	1.52	0.62	109	64	3.1	1.8

NOTE—Table 3 is published in its entirety in the electronic edition of the *Astrophysical Journal*. A portion is shown here for guidance regarding its form and content.

where $T_L = h\nu_{10}/k_B$ and $T_{bg}=2.725$ K. The total column density of ^{13}CO is

$$N(^{13}\text{CO}) = N_{1,thin} Z \exp(hB_o J(J+1)/k_B T_{ex}) / (2J+1) \quad (7)$$

where B_o is the rotational constant for ^{13}CO , and Z is the partition function, which accounts for population in other states

$$Z = \sum_{J=0}^{\infty} (2J+1) \exp(-hB_o J(J+1)/k_B T_{ex}) \quad (8)$$

Finally, to convert to molecular hydrogen column density, $N(\text{H}_2) = N(^{13}\text{CO})[\text{H}_2/^{13}\text{CO}]$, we assume a constant excitation temperature of 8 K and a H_2 to ^{13}CO abundance ratio of 4.1×10^5 for all clouds. This value for T_{ex} is based on studies by [Heyer et al. \(2009\)](#) and [Roman-Duval et al. \(2010\)](#) who found mean T_{ex} values of 7-8 K derived from ^{12}CO data for large samples of clouds. The assigned abundance value is based on mean abundance values for nearby clouds using infrared-derived extinction as a proxy for H_2 column density ([Lada et al. 1994](#); [Pineda et al. 2008, 2010](#); [Ripple et al. 2013](#)). This leads to a conversion between ^{13}CO integrated intensity and molecular hydrogen column density of $3.9 \times 10^{20} \text{ cm}^{-2}/(\text{K km s}^{-1})$ that is a required argument in the CPROPS program to calculate mass. The cloud mass is then

$$M_{\text{cloud}} = 3.9 \times 10^{20} \mu m_H D^2 \int d\Omega \int dv T_B(l, b, v) \quad (9)$$

where D is the distance and the integrals are over the solid angle, Ω_{cl} , and velocity range for the set of cloud voxels.

There are several sources of uncertainty in the MC mass. These include distance, abundance and T_{ex} variations, and random errors owing to the observations. This last component is small compared to the other sources and is ignored. For ^{13}CO , we estimate the uncertainty of the conversion factor from integrated intensity to $N(^{13}\text{CO})$ by varying the assumed excitation temperature from 4 to 16 K in steps of 2 K. The fractional root mean square of values about the adopted value for 8 K is 27%. The variations of ^{13}CO abundance, $[\text{H}_2/^{13}\text{CO}]$ both within clouds and from cloud-to-cloud in the solar neighborhood is $\sim 30\%$ ([Ripple et al. 2013](#)). These uncertainties are included in the values in Table 3, but distance errors are not (see Appendix).

Assuming a spherical cloud and a power law density profile with index of 1, the CPROPS package calculates the virial mass, M_{vir} , from the expression,

$$M_{\text{vir}} = 1040 \delta v^2 r_{\text{cloud}} M_{\odot} \quad (10)$$

where δv is the 1-dimensional velocity dispersion in km s^{-1} and r_{cloud} is the effective radius of the cloud in parsecs. The coefficient can be found in [MacLaren et al. \(1988\)](#) after converting from FWHM to δv . The virial parameter, $\alpha = M_{\text{vir}}/M_{\text{cloud}}$, offers a coarse measure of the boundedness of the cloud, assuming there is no significant external pressure. The mean volume density of the cloud, n_{cloud} , is derived from the M_{cloud} and r_{cloud} , assuming a spherical cloud geometry, $n_{\text{cloud}} = 3M_{\text{cloud}}/4\pi\mu m_H r_{\text{cloud}}^3$.

3.3.2. Dense Gas Mass

Dense gas properties are estimated for each MC using source fluxes and sizes from the BGPS Version 2.1 source catalog. The relation between gas mass and dust continuum flux is given by the expression

$$M_{\text{dense}} = \frac{S_{1.1} D^2 (\rho_g / \rho_d)}{B_{\nu}(T_{\text{dust}}) \kappa_{\text{dust},1.1}}, \quad (11)$$

where $S_{1.1}$ is the 1.1 mm flux density, D is the distance, $\kappa_{\text{dust},1.1}$ is the dust opacity at 1.1 mm per dust mass, assumed to be $1.14 \text{ cm}^2 \text{ g}^{-1}$ ([Ossenkopf & Henning 1994](#)), and ρ_g / ρ_d is the gas-to-dust mass ratio, taken to be 100 ([Hildebrand 1983](#)). Using this expression, we derive the mass and associated uncertainties using a Monte Carlo simulation that assumes Gaussian errors on the flux density and a Gaussian distribution of dust temperatures with a mean of 20 K and a standard deviation of 8 K ([Battersby et al. 2011](#); [Ellsworth-Bowers et al. 2015](#)). The total dense gas mass for each MC is estimated from the sum of the masses for all Bolocam sources within the cloud mask with and without v_{LSR} information. We also derive the dense gas mass fraction (DGMF) corresponding to the ratio of the mass traced by BGPS 1.1 mm sources to the mass of the MC as traced by ^{13}CO emission,

$$DGMF = \frac{M_{\text{dense}}}{M_{\text{cloud}}}$$

Properties of the dense gas component are given in Table 4.

Table 4. BGPS-Derived Dense Gas Properties

WISE Name	M_{dense}	$\sigma(M_{\text{dense}})$	r_{dense}	$\sigma(r_{\text{dense}})$	DGMF	$\sigma(\text{DGMF})$
	(M $_{\odot}$)		(pc)			
G031.561+00.376	1143.2	663.3	0.8	0.1	0.017	0.012
G032.077-00.230	2503.7	1337.0	4.0	0.6	0.024	0.016
G032.030+00.048	15865.8	6177.0	5.6	0.8	0.088	0.049
G032.272-00.226	3099.3	1254.4	3.4	0.5	0.396	0.226
G032.473+00.204	3942.9	1548.8	5.5	0.8	0.039	0.022
G032.582+00.001	2351.8	1179.0	4.4	0.7	0.058	0.037
G032.587-00.330	150.8	118.8	2.3	0.3	0.007	0.006
G032.733+00.209	23918.2	9357.0	6.5	1.0	0.256	0.144
G032.870-00.427	5439.9	1554.3	5.8	0.6	0.075	0.037
G033.419-00.005	5440.5	2134.5	5.3	0.8	0.112	0.063
G033.643-00.229	-99.9	-99.9	-99.9	-99.9	-99.900	-99.900
G033.809-00.190	7411.8	2225.8	6.9	0.7	0.321	0.162
G033.941-00.039	2954.6	1155.2	4.2	0.6	0.138	0.077
G034.041+00.052	2547.2	1033.1	6.5	1.0	0.077	0.044
G034.089+00.438	4360.4	1741.7	4.3	0.7	0.357	0.203

NOTE—This table is published in its entirety in the electronic edition of the *Astrophysical Journal*. A portion is shown here for guidance regarding its form and content.

4. CLASSIFICATION OF MCS

We classified our sample of star forming MCs into three distinct groups based on the locations of the associated H II regions with respect to the molecular cloud. Group 1 MCs have associated radio continuum emission whose solid angle is mostly circumscribed by the boundary of ^{13}CO emission. There are 37 MCs in Group 1. For Group 2 MCs, the radio continuum emission partially overlaps or is contiguous with ^{13}CO boundaries but the RRL sources lie outside the clouds. The left panel of figure 2 shows a Group 1 cloud, while the right panel shows a Group 2 cloud. There are 21 MCs in Group 2. Finally, Group 3 clouds are MCs in which the radio continuum emission is well displaced from the ^{13}CO boundaries. The association of the MC with the H II region is most uncertain for Group 3 sources. With no angular overlap with the MC, the association is solely based on the chosen spatial and velocity offsets. There are only 8 MCs in this group. Due to the small number and the uncertainty of associating gas and star formation in this group, we exclude Group 3 MCs from all further analysis.

The classification into groups in this study has some overlap with the classification used by Fukui et al. (1999) and Kawamura et al. (2009) (K09), but our spatial resolution is higher than that of K09 so we examine associations between MCs and star formation on smaller spatial scales but also require similar velocities to account for line of sight confusion. Nevertheless, our classifications likely correspond to a similar evolutionary sequence in which Group 1 is the earliest stage of massive star formation (Type II of K09), Group 2 describes the initial feedback from massive stars, and Group 3 is a very late stage in which the original cloud has been mostly photoionized or dispersed, leaving only small fragments, similar to Type III clouds in the K09 classification.

To explore whether Group 1 and Group 2 sources differ in the main properties we are considering, we computed averages and standard deviations (in the log for quantities with large ranges) for the two groups; these are shown in Table 5. The two groups have very similar averages for M_{cloud} , M_{dense} , n_{cloud} , r_{cloud} , and SFE ($\text{SFR}/M_{\text{cloud}}$). Group 2 clouds may have somewhat larger mean values for α and somewhat smaller values for DGMF. Because the differences are not statistically significant, we do not distinguish the two groups in the rest of the analysis.

5. TESTING STAR FORMATION RELATIONS

The question we address in this section is the following: which properties of the ISM best predict the SFR for the clouds in this sample? The first proposed relation (Schmidt 1959, 1963) suggested that the SFR would be a function of the density of gas. For extragalactic studies, the surface densities of star formation rate (Σ_{SFR}) and gas (Σ_{gas}) are easier to measure than are volume densities. Studies of other galaxies found that $\Sigma_{\text{SFR}} \propto \Sigma_{\text{gas}}^{1.4}$ provided

Table 5. Comparison of Groups 1 and 2

Property	Group 1 Average	Group 2 Average	Group 1 Number	Group 2 Number
$\langle \log M_{\text{cloud}} \rangle$	4.58 ± 0.48	4.43 ± 0.57	32	19
$\langle \log M_{\text{dense}} \rangle$	3.49 ± 0.98	3.19 ± 1.55	30	14
$\langle \log n_{\text{cloud}} \rangle$	1.97 ± 0.38	2.01 ± 0.63	32	19
$\langle r_{\text{cloud}} \rangle$	12.6 ± 6.6	12.5 ± 8.2	32	19
$\langle \alpha \rangle$	1.44 ± 1.11	1.86 ± 1.26	32	19
$\langle DGMF \rangle$	0.12 ± 0.11	0.06 ± 0.045	30	14
$\langle \log SFE \rangle$	-2.93 ± 0.54	-2.89 ± 0.54	32	19

a good fit for a wide range of galaxies (Kennicutt 1998). When only molecular gas is considered, linear relations are generally found ($\Sigma_{\text{SFR}} \propto \Sigma_{\text{gas}}$) (Bigiel et al. 2008; Leroy et al. 2013), even for the outer regions of galaxies, where the gas is predominantly atomic (Schruba et al. 2011). Studies of galaxies on sub-kiloparsec scales have shown that star formation is associated with molecular gas (e.g., Leroy et al. 2013). Within the Milky Way, studies with sub-parsec resolution show that star formation is further concentrated within relatively dense or opaque parts of molecular clouds (Lada et al. 2010; Heiderman et al. 2010).

In this section, we use our sample of star forming regions to test some of the proposed models for how SFRs are determined in MCs. In doing so, we consider integrated properties, such as cloud mass, mass of dense gas, or cloud mass per free fall time as variables in the following equation, where X represents the variable in question.

$$\text{SFR} = AX^n \quad (12)$$

Because of the large range of parameters, and to be consistent with previous studies, we generally fit the logarithmic version of these relations.

$$\log \text{SFR} = \log A + n \log X \quad (13)$$

We examine the various relations that are used in extragalactic work or that have been proposed by theorists for clouds in the Milky Way selected to have substantial star formation. We use the SFR from the mid-infrared data and consider only clouds with a SFR of at least $5 M_{\odot} \text{ Myr}^{-1}$, as discussed earlier. The basic sample thus includes 51 sources. The samples for other variables are somewhat smaller depending on which data are available. For the dense gas relations, only 44 sources are available because not all clouds had BGPS sources. We calculate the Pearson correlation coefficient to evaluate the probability that the measured relationship could emerge from a population of random numbers. If the correlation is significant (using Pearson r , a 3σ correlation requires $|r| > 3/\sqrt{N_s - 1}$, where N_s is the sample size), we fit the data to the model in equation 13 to determine the parameters, $\log(A)$ and n , considering errors in both variables using the MPFITEXY routine (Williams et al. 2010), which depends on the MPFIT package (Markwardt 2009). In this model-fitting program, the intrinsic scatter of the data about the model is included in the error-weighting of the data. If necessary, this intrinsic scatter is iteratively modified so that the reduced χ^2 value of the fit is about unity. The scatter of points is characterized by the root mean square of the displacement of $\log(\text{SFR})$ values from the best fit line for each value of X . The parameters from the fits are given in Table 6. The column labeled DOF shows the sample size minus the number (2) of fit parameters.

Table 6. Star Formation Rate Fits

Variable	$\log A$	n	DOF	χ^2	RMS	Pearson r
Cloud Mass	-1.38 ± 0.56	0.66 ± 0.12	49	0.997	0.46	0.49
Dense Mass	-2.12 ± 0.62	1.09 ± 0.18	42	1.019	0.52	0.58
$M_{\text{cloud}}/t_{\text{ff}}$	-5.61 ± 1.60	1.80 ± 0.39	48	0.919	0.75	0.55
$t_{\text{ff}}/t_{\text{dyn}}^a$	0.13

^aIn this case the quantity being fitted is ϵ_{ff} , rather than SFR

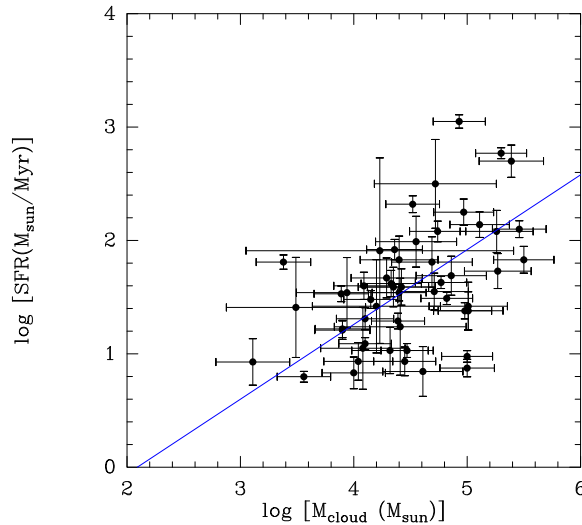
5.1. *Star Formation Rate versus Cloud Mass*

Figure 3. The relation between SFR and M_{cloud} . The line is the linear least-square fit to the data.

The first and the simplest proposition is that SFR depends solely on the total mass of the MC (M_{cloud}). This is the extragalactic star formation relation applied on the cloud scale. In this case $X = M_{\text{cloud}}$, as determined by the ^{13}CO emission. Figure 3 shows the SFR versus M_{cloud} . The dotted lines represent the linear least-square fits to the log of the data. The fit parameters to Equation 13 gives the slope $n = 0.66 \pm 0.12$, sub-linear by nearly 3σ (see Table 6). The relation for the Galactic Plane clouds is thus considerably flatter than the linear relation found for other galaxies, averaging over kpc scales (Bigiel et al. 2008; Leroy et al. 2013; Schruba et al. 2011).

5.2. *Star Formation Rate versus Dense Gas Mass*

A tighter relation has been observed in other galaxies between SFR and dense gas mass. Gao & Solomon (2004) observed a tight linear relationship between $L(\text{IR})$ and $L(\text{HCN})$ in a sample of infrared galaxies. Wu et al. (2005) found that the relationship is extended to the scale of Galactic dense clumps. These studies and the study of nearby molecular clouds led to the proposal that molecular gas above some density can form stars efficiently (Goldsmith et al. 2008; Lada et al. 2010; Heiderman et al. 2010). The star-formation threshold model (Lada et al. 2012; Evans et al. 2014) states that the SFR in MCs is best predicted by the amount of dense gas above some threshold density. In this case, $X = M_{\text{dense}}$, as measured by the sum of masses of the BGPS sources within the cloud, with the caveat that BGPS sources are lower density and more like clouds at large distances owing to spatial filtering to remove atmospheric emission (Dunham et al. 2011).

Comparing SFR and M_{dense} in our sample yields a nearly linear relation ($n = 1.09 \pm 0.18$) with a Pearson correlation coefficient of 0.58. Figure 4 shows the result of the relation between SFR and M_{dense} .

5.3. *SFR versus $M_{\text{cloud}}/t_{\text{ff}}$*

The free-fall model states that the SFR depends on the molecular mass over the free-fall time (Krumholz & McKee 2005; Krumholz et al. 2012):

$$SFR = f_{H_2} \epsilon_{\text{ff}} \times \frac{M_{\text{gas}}}{t_{\text{ff}}}, \quad (14)$$

where f_{H_2} is the fraction of molecular gas compared to the total gas mass, $\epsilon_{\text{ff}} = t_{\text{ff}}/t_{\text{dep}}$ is the star formation efficiency per free-fall time, the gas depletion time is t_{dep} , and the free-fall time is

$$t_{\text{ff}} = \sqrt{\frac{3\pi}{32G\rho}}. \quad (15)$$

For MCs, where only molecular gas is concerned, the relation becomes

$$SFR = \epsilon_{\text{ff}} \times \frac{M_{\text{cloud}}}{t_{\text{ff}}}. \quad (16)$$

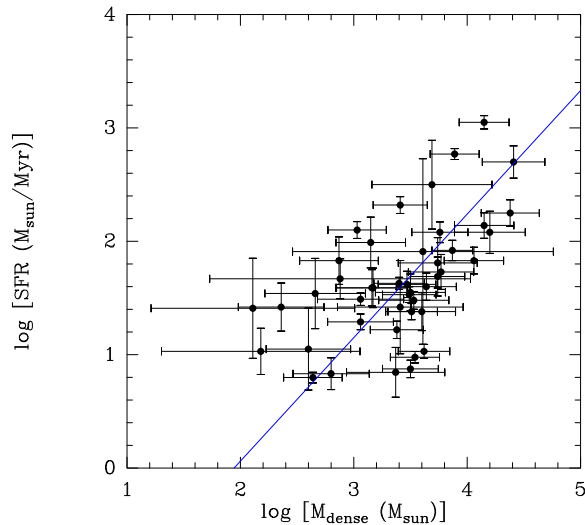


Figure 4. The relation between SFR and M_{dense} . The line is the linear least-square fit to the data.

Comparing data from nearby clouds to other galaxies, [Krumholz et al. \(2012\)](#) estimated an approximately constant ϵ_{ff} of 0.01. This value is aligned with theoretical predictions ([Krumholz & McKee 2005](#); [Padoan et al. 2012](#)).

We tested the free-fall model with our cloud sample by using the total MC mass from ^{13}CO and using the average density for t_{ff} . The result is shown in Figure 5. The red line represents the relation in Equation 16 with $\epsilon_{\text{ff}} = 0.01$. The fit to the data shows a super-linear relation with $n = 1.80 \pm 0.39$. The Pearson correlation coefficient is 0.55. Generally speaking, including the free-fall time did not improve the relation compared to using M_{cloud} , and the super-linear fit is not consistent with the hypothesis of [Krumholz et al. \(2012\)](#).

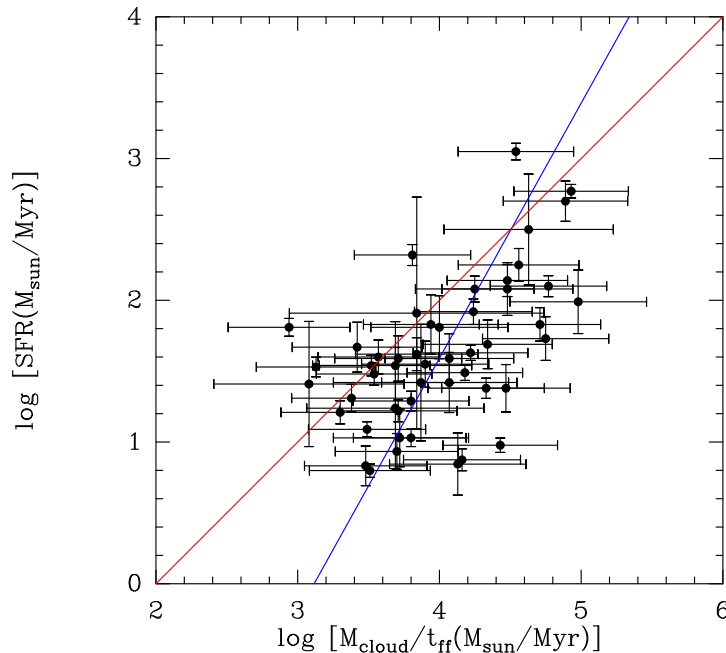


Figure 5. The relation between SFR and mass over free-fall time. The blue line is the linear least-square fit to the data, and the red line represents the free-fall model with $\epsilon_{\text{ff}} = 0.01$.

5.4. ϵ_{ff} versus $t_{\text{ff}}/t_{\text{dyn}}$

As summarized by [Padoan et al. \(2014\)](#), simulations of turbulent molecular clouds indicate that the speed of star formation, measured by ϵ_{ff} , should depend on the virial parameter. In particular [Padoan et al. \(2012\)](#) show that

turbulent simulations closely follow the following relation.

$$\epsilon_{\text{ff}} = \epsilon_{\text{wind}} e^{-1.6 t_{\text{ff}}/t_{\text{dyn}}} \quad (17)$$

where ϵ_{wind} is the core to star efficiency, taken to be about 0.5 due to winds removing material, and $t_{\text{dyn}} = r_{\text{cloud}}/\sigma_{\text{v},3\text{D}}$, and $\sigma_{\text{v},3\text{D}} = \sqrt{3}\sigma_{\text{v},1\text{D}}$. The variable $t_{\text{ff}}/t_{\text{dyn}}$ is simply related to the virial parameter by

$$t_{\text{ff}}/t_{\text{dyn}} = 0.86\sqrt{\alpha} \quad (18)$$

where α is the virial parameter.

The data are plotted in Figure 6, along with the prediction of Padoan et al. (2012). The data show no significant correlation (Pearson correlation coefficient of 0.13) and lie on average a factor of 55 below the model predictions. The mean efficiency ϵ_{ff} for M_{cloud} is 0.008, comparable to the Krumholz et al. (2012) value of 0.01. For this sample, $\langle\alpha\rangle = 1.6 \pm 1.2$; if we use that value in equations 17 and 18, they would predict $\epsilon_{\text{ff}} = 0.09$, more than 10 times the observed mean value.

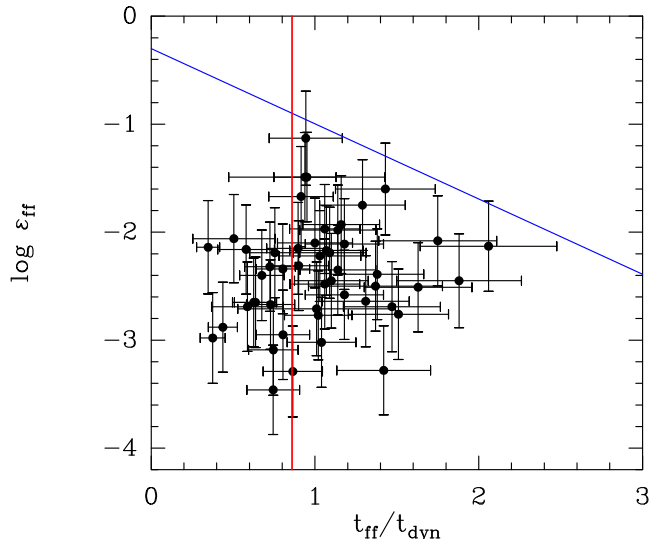


Figure 6. The relation between ϵ_{ff} and free-fall time over dynamical (crossing) time. The blue line is the prediction of the model of Padoan et al. (2012). The red vertical line indicates $\alpha = 1$.

5.5. Summary of Star Formation Relationships

Comparison of the values in Table 6 shows that all three variables (M_{cloud} , M_{dense} , $M_{\text{cloud}}/t_{\text{ff}}$) have similar correlation coefficients. All the correlations are significant at the 3σ level. Equivalently, we can exclude the null hypothesis that the correlations arise from a random distribution of variables with a high level of probability. Only the correlation with M_{dense} is consistent with a linear relation. The fit to SFR versus M_{cloud} shows a slope much flatter (0.66 ± 0.12) than the usual values of 1.0 to 1.5. Theory predicts a linear relation between SFE and $M_{\text{cloud}}/t_{\text{ff}}$, but the slope we find (1.80 ± 0.39) differs by more than 2σ from theoretical expectation.

Another theoretical prediction is that the star formation efficiency per free-fall time should decrease exponentially with the ratio of the free-fall time to the dynamical time. As shown in Figure 5, there is no significant correlation in our data and the values lie well below the predictions.

Comparing SFR and M_{cloud} we found considerable scatter. This scatter has been observed and quantitatively explained in several studies (Onodera et al. 2010; Schruba et al. 2010; Kruijssen & Longmore 2014). One explanation is that the strong correlation observed when looking at the scale of galaxies is due to averaging over variations in different star forming regions' properties. When looking at the scale of MCs, the properties of MC such as the evolutionary stages contribute to the scatter in the relation between mass and SFR. Even in our sample where only sources with overlap between molecular gas and star formation are selected (thus leaving out the earlier stages such as IRDC and later stages where stellar feedback disrupts the clouds), the scatter in SFR and M_{cloud} relations is large. In previous work, we have shown that averaging over larger regions in our Galaxy reduces the scatter (Vutisalchavakul et al. 2014).

6. COMPARISON TO NEARBY CLOUDS

Now that we have extended the study of star formation relations to more distant regions forming more massive stars in the Milky Way, we can compare the results to those for nearby clouds (Evans et al. 2014; Heiderman et al. 2010). Those authors considered star formation relations **within** the nearby clouds, but we lack the resolution to do that for the Galactic Plane clouds. In addition, Lada et al. (2013) highlighted the differences between star formation relations **within** and **between** clouds, and Parmentier (2016) has summarized the issues in comparing surface densities of SFR and gas between nearby and more distant clouds. Furthermore, plotting SFR versus mass introduces a correlation because both are proportional to the square of distance. Cognizant of these issues, we focus on SFE (distance cancels out) and deal with the masses contained within the entire cloud or a dense clump within the cloud, rather than using surface density *within* a cloud or clump.

First, we consider whether comparable regions have been selected. For the nearby clouds, a region above a threshold extinction, generally $A_V = 2$ mag, was selected for surveys of YSOs (Evans et al. 2009). For this paper, the clouds were defined by maps of $^{13}\text{CO } J = 1 \rightarrow 0$ emission, followed by extrapolation to zero emission. Our estimates of an effective threshold for the Galactic Plane clouds range from $A_V = 1$ to 3 mag. This may be in addition to extinction of several magnitudes associated with layers of atomic and molecular gas exterior to the ^{13}CO boundary limited by photodissociation. The mean density of the selected clouds for the Galactic Plane sample is about 300 cm^{-3} , lower than the average for the nearby clouds of about 800 cm^{-3} .

The measure of “dense” gas in the nearby clouds was an extinction threshold of $A_V = 8$ mag. Using the typical rms noise in the BGPS survey of 0.1 mJy/beam (Ginsburg et al. 2013), a dust temperature of 20 K, and OH5 dust opacities (Ossenkopf & Henning 1994), a 3σ detection limit translates to $A_V = 7$ mag, comparable to that used to define dense regions in the nearby clouds. A second analysis, using the actual distribution of rms noise in the BGPS yields a slightly smaller threshold, $A_V = 4.6$ mag at 90% completeness (B. Svoboda, pers. comm.).

However, the mean volume density of the BGPS sources in the Galactic Plane sample is only 10^3 cm^{-3} , substantially lower than the mean density of the regions above $A_V = 8$ for the nearby clouds ($\langle n \rangle = 6 \times 10^3 \text{ cm}^{-3}$). Thus, the galactic plane “dense” gas is not as dense as that defined in the nearby clouds. For more distant targets, where the molecular clouds may subtend angles less than $3'$, the mass and densities may reflect the full cloud rather than high density fragments (Dunham et al. 2011; Battisti & Heyer 2014).

A common feature of all observational studies of star formation is a low star formation efficiency. Only a small fraction of the gas in galaxies is actively forming stars. The fractional mass of young stars in molecular clouds is around 5% (Evans et al. 2009; Dunham et al. 2015). In the extragalactic context, star formation efficiency (SFE) refers in fact to the slow *pace* of star formation, the star formation rate per unit mass, as reflected in t_{dep} , the inverse of SFE, being 1-2 Gyr. Parallel to our equations for SFR, we consider relations for the SFE and t_{dep}

$$\text{SFE} = \text{SFR}/X = AX^{n-1} \quad (19)$$

$$t_{\text{dep}} = X/\text{SFR} = A^{-1}X^{1-n} \quad (20)$$

and their logarithmic versions.

Table 7. Star Formation Efficiencies

Variable	Log SFE(nearby)	Standard Deviation	Log SFE(GP)	Standard Deviation
Cloud Mass	-2.07	0.83	-2.91	0.53
Dense Mass	-1.61	0.23	-1.74	0.50
$M_{\text{cloud}}/t_{\text{ff}}$	-1.90	0.45	-2.38	0.49

We plot the SFR per entity for the three main entities used to predict SFR in Figures 7 to 9. The three entities are cloud mass (M_{cloud}), dense gas mass (M_{dense}), and cloud mass per free-fall time ($M_{\text{cloud}}/t_{\text{ff}}$). In extragalactic parlance, the first two are “star formation efficiencies”, or the reciprocal of the depletion time, measured in Myr. The last is unitless and equal to ϵ_{ff} . We will refer to these generically as the SFE. The black points are from the nearby clouds, while the red points are from this paper. The means and standard deviations (both in the log) are given in Table 7.

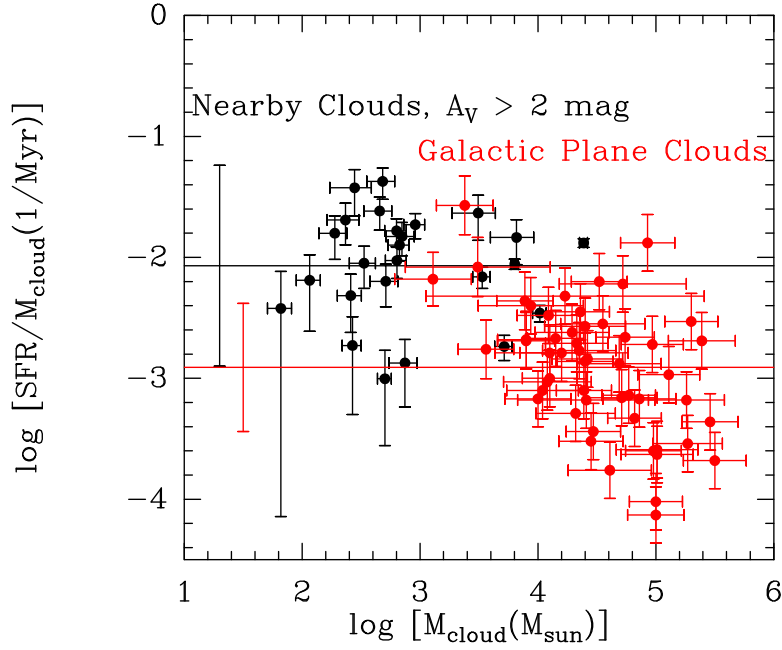


Figure 7. Plot of the logarithm of SFR per mass of molecular gas vs. the logarithm of the mass of molecular gas. The red points are from this paper and the black points are for nearby clouds, taken from [Evans et al. \(2014\)](#). The black horizontal line is the mean value for the nearby clouds and the red horizontal line is the mean value for the data in this paper. The error bars at the far left are the standard deviations of $\log(\text{SFE})$.

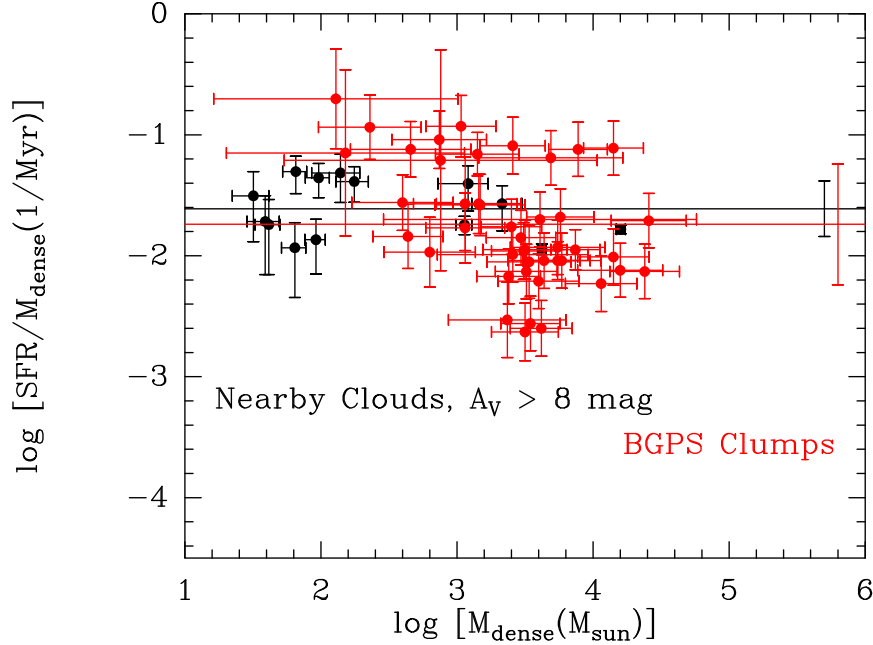


Figure 8. Plot of the logarithm of SFR per mass of dense gas vs. the logarithm of the mass of dense gas. The red points are from this paper and the black points are for nearby clouds, taken from [Evans et al. \(2014\)](#). The black horizontal line is the mean value for the nearby clouds and the red horizontal line is the mean value for the data in this paper. The error bars at the far right are the standard deviations of $\log(\text{SFE})$.

The following facts are apparent. The standard deviations in the SFE for Galactic Plane clouds are comparable (about 0.5 dex) for all the relations (the figures are plotted on the same scales so the eyeball estimate of the scatter is meaningful). The mean of the SFE for the Galactic Plane clouds is lower by 0.8 in the log than that for the nearby clouds when cloud mass is used, but very similar (lower by 0.13 in the log) when dense gas mass is used.

The agreement of the SFE for the dense gas relation is striking because the method to estimate the SFR for

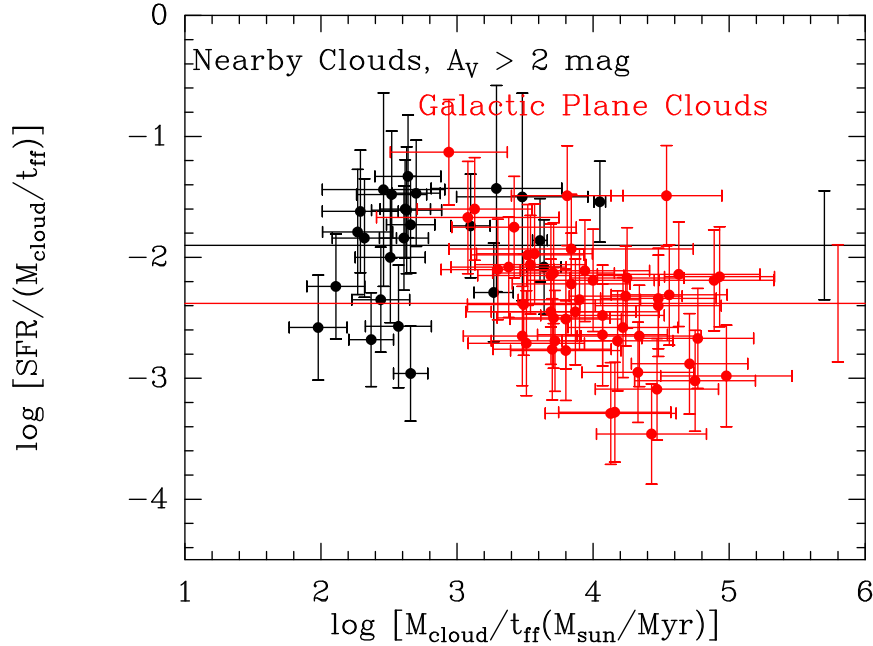


Figure 9. Plot of the logarithm of SFR divided by the cloud mass over the free-fall time vs. the logarithm of the cloud mass over the free-fall time. The red points are from this paper and the black points are for nearby clouds, taken from [Evans et al. \(2014\)](#). The black horizontal line is the mean value for the nearby clouds and the red horizontal line is the mean value for the data in this paper. The error bars at the far right of these lines are the standard deviation of the $\log(\text{SFR}/(M_{\text{cloud}}/t_{\text{ff}}))$ for the two data sets.

the Galactic Plane sample is very different (MIR emission) from that used for the nearby clouds (YSO counts) so disagreement could be expected. Indeed, we know that MIR emission seriously underestimates the SFR for the nearby clouds, and we might expect an underestimate of 0.3 to 0.5 in the log for the Galactic Plane sample, based on the discussion in §3.2.3. The agreement for the dense gas encourages us that the Galactic Plane sources have SFR sufficiently high that the MIR tracer is not greatly underestimating the SFR. The alternative explanation, that the SFR and the dense gas mass are both underestimated by the same amount, is implausible because the mean density of the Galactic Plane clumps is less than that of the dense clumps in the nearby clouds, as noted above. If anything, the masses of gas as dense as those in the nearby clouds is over-estimated in the Galactic Plane clouds.

The SFE for the Galactic Plane clouds is about 10^{-3} Myr^{-1} , which is consistent with a depletion time of 1 Gyr, similar to that for galaxies as a whole. [Murray \(2011\)](#) used WMAP data to find the most luminous H II regions in the Galaxy and to compute star formation rates. His sample is clearly biased to the regions with the highest star formation rates. After connecting these H II regions to molecular gas using catalogs of GMCs, he computed star formation efficiencies. For consistency, we used our equation to recompute his star formation rates, but they are only slightly lower than the rates he gave. His data are added in Figure 10 as the blue points; they have a mean SFE similar to that of the nearby clouds, and they further extend the dispersion among Galactic Plane clouds. We cannot do a full analysis with Murray’s sources as no uncertainties are given, the identification with molecular gas is not clearly described, and there is no information on the dense gas. However, a simple mean value of SFE including his sample and ours yields $\langle \log \text{SFE} \rangle = -2.52 \pm 0.72$ where SFE is measured in Myr^{-1} as usual, bringing the mean for the Galactic Plane clouds closer to that for the nearby clouds.

The main feature that emerges from the data is a large dispersion in SFR per cloud mass for both the nearby and the Galactic Plane clouds. The mean SFE depends on sample selection. When the dense gas mass is used to determine SFE, the dispersion is less and the mean values for nearby and Galactic Plane clouds agree. Differences between the nearby clouds and the Galactic Plane clouds may be related to different feedback effects. Other than the Orion cloud, the local regions are primarily generating low mass stars because the IMF is not fully sampled. In such low mass star forming regions, protostellar outflows are the primary feedback process. Such outflows can perturb the cloud structure over scales up to several parsecs over a restricted volume set by the jet opening angle. However, their effect on the overall cloud structure is limited and incapable of suppressing the SFE. Massive young stars provide a much stronger energy input to the cloud primarily through far-UV radiation fields that drive expanding H II regions ([Matzner 2002](#); [Dale et al. 2014](#)). These processes can impact the SFE by photoionizing part of the cloud or simply modifying the

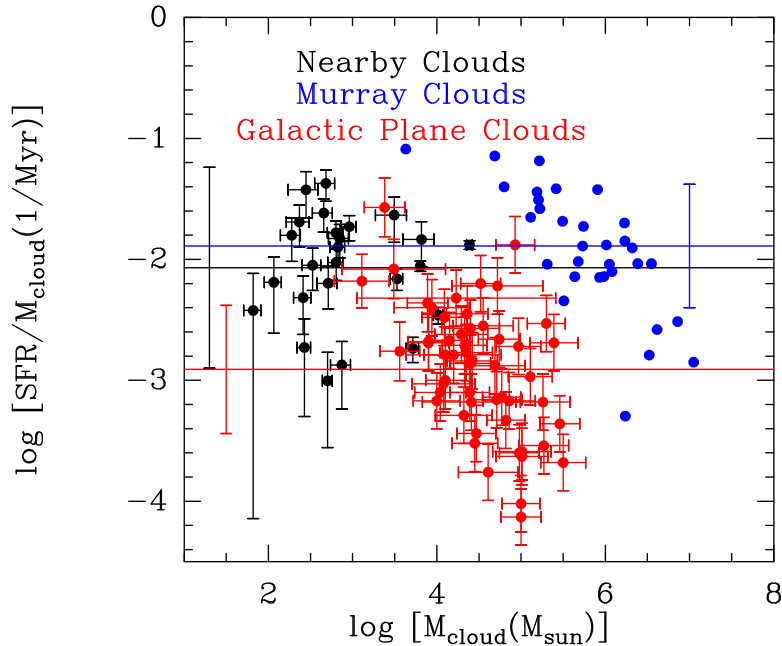


Figure 10. Plot of the logarithm of SFR per mass of molecular gas vs. the logarithm of the mass of molecular gas. The red points and black points are as in the previous figure. The blue points are from Murray (2011). The blue horizontal line is the mean value and error bar at the far right is the standard deviation for the data from Murray (2011).

conditions to make them less suitable for star formation. Some support for this might be found in the apparently higher mean value of α in the Group 2 clouds (Table 5) but the dispersion is quite large. In addition, the mean values for α for the nearby clouds and the Galactic Plane clouds are indistinguishable. The most likely effect of the massive stars is to confuse observational measures by removing or ionizing the molecular gas, leading to Group 2 or 3 sources, configurations which are not seen in the nearby clouds.

7. COMPARISON TO EXTRAGALACTIC RESULTS

Studies of other galaxies have explored the same questions as have been addressed in this paper. In this section, we compare those results to those in the Milky Way. We continue to use the SFE to avoid the strong apparent correlation introduced by the fact that both mass and SFR generally scale as size, hence distance, squared. For the extragalactic studies, clouds are generally not resolved, so we use M_{mol} to represent the aggregate mass in molecular gas, while M_{dense} continues to represent the aggregate mass of dense gas.

The first comparison is for overall molecular gas. Figure 11 plots the mean and standard deviation (in log space) of the SFE for the nearby clouds and the Galactic Plane clouds, along with data from other studies. The green points show results from spatially resolved studies of nearby galaxies. The lowest green point is from Leroy et al. (2013), who summarized the HERACLES data on 30 “nearby” ($d < 22$ Mpc) disk galaxies. The SFE plotted for the galaxies is actually the log of $1/\langle t_{\text{dep}} \rangle$, but calculation of $\langle SFE \rangle$ from their data tables produces a nearly identical result. The mass scale is that of their resolution, obtained from the surface density and resolution in their Table 1, converted to mass, converted to logs, and averaged, resulting in a characteristic $\log(M_{\text{mol}})$ of 6.63 ± 0.59 . The other two green points are from the study of M51 with 1 kpc resolution as presented by Chen et al. (2015); the highest green point is for the outer parts of M51, while the lower one at higher masses is from the inner 1.66 kpc. Finally, whole galaxies can be plotted, based on a sample of 115 disk galaxies in Liu et al. (2015). The normal galaxies are plotted in blue and the (U)LIRGs are plotted in cyan. The higher cyan point uses the (U)LIRG conversion from CO to molecular gas while the lower point uses the same conversion as used for the normal galaxies. The plot shows a decline in SFE from the nearby clouds to the Galactic Plane clouds to the extragalactic regions. The standard deviation in the SFE also decreases, presumably due to averaging over more and more star formation regions (cf Kruijssen & Longmore 2014; Vutisalchavakul et al. 2014). A rise in SFE is seen for the (U)LIRGs, especially if the lower, (U)LIRG, value for the conversion factor is used, for which the SFE exceeds even the value in the nearby clouds.

The same plot can be made for the dense gas, again using averages and standard deviations in logs, using masses based on HCN emission and

$$M_{\text{dense}}(M_{\odot}) = 10L_{\text{HCN}} \quad (21)$$

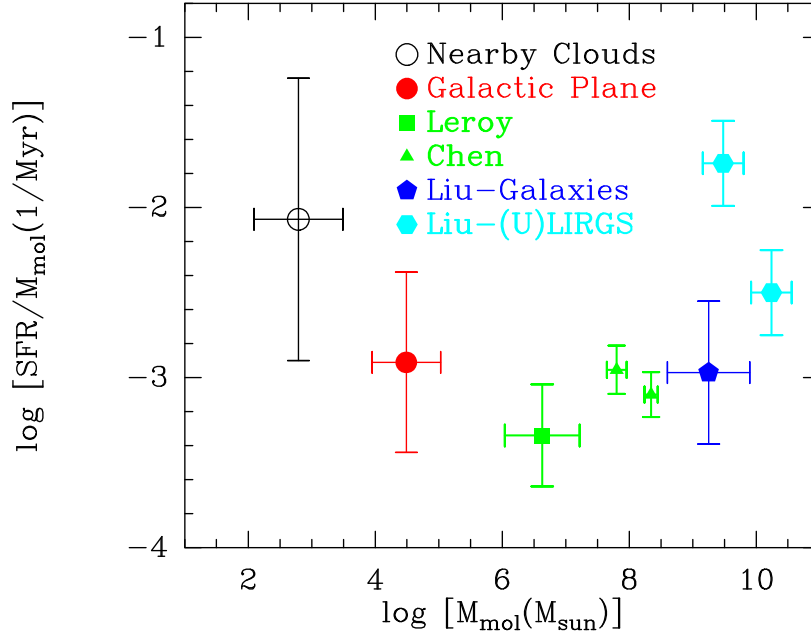


Figure 11. Plot of the logarithm of SFR per mass of molecular gas vs. the logarithm of the mass of molecular gas, showing averages and standard deviations (in the logs). The red filled circle is from this paper and the open black circle is for the nearby clouds, taken from [Evans et al. \(2014\)](#). Three green points are plotted for resolved studies in nearby galaxies. The lowest point (square) is from [Leroy et al. \(2013\)](#) who observed with resolutions from 0.2 to 1.4 kpc. The other two points (triangles) are from [Chen et al. \(2015\)](#), who observed M51 with 1 kpc resolution; the higher point is for the outer galaxy and the lower point is for inner ($r < 1.66$ kpc) part of M51. The blue point (pentagon) represents the normal galaxies while the cyan points (hexagons) represent the (U)LIRGs from [Liu et al. \(2015\)](#). Two values are plotted, the higher one using the conversion from CO to molecular gas of $\alpha_{\text{CO}} = 0.8 M_{\odot}(\text{K km s}^{-1}\text{pc}^2)^{-1}$, while the lower one uses the same value as for the normal galaxies, $\alpha_{\text{CO}} = 4.6 M_{\odot}(\text{K km s}^{-1}\text{pc}^2)^{-1}$.

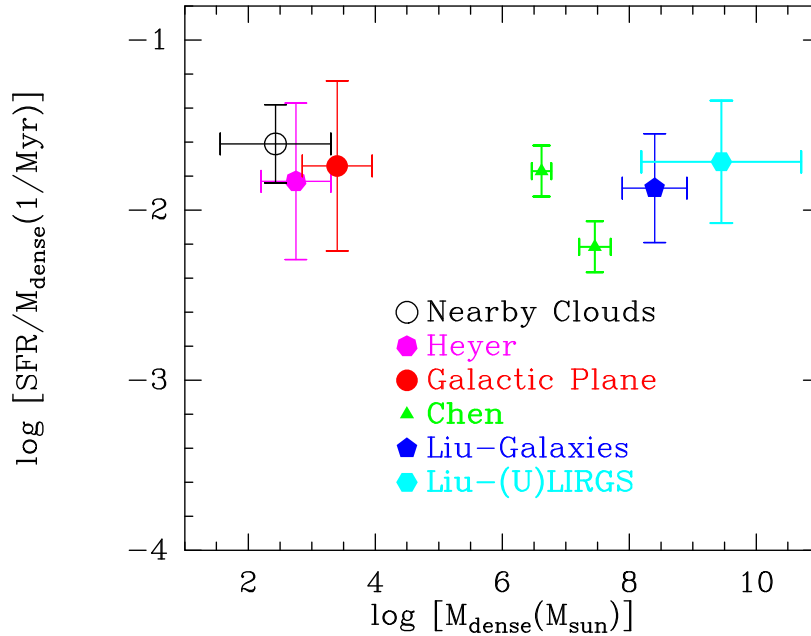


Figure 12. Plot of the logarithm of SFR per mass of dense gas vs. the logarithm of the mass of dense gas, showing averages and standard deviations (in the logs). The red point (filled circle) is from this paper and the black point (open circle) is for the nearby clouds, taken from [Evans et al. \(2014\)](#). The magenta point (heptagon) comes from [Heyer et al. \(2016\)](#). The two green points (triangles) are from [Chen et al. \(2015\)](#), who observed M51 with 1 kpc resolution; the higher point is for the outer galaxy and the lower point is for inner ($r < 1.66$ kpc) part of M51. The blue point (pentagon) represents the whole, normal galaxies while the cyan point (hexagon) represents the whole (U)LIRGs, both from [Liu et al. \(2015\)](#).

where L_{HCN} is the observed luminosity of HCN $J = 1 \rightarrow 0$ emission in $\text{K km s}^{-1} \text{ pc}^2$ (Liu et al. 2015). The (U)LIRGs in Liu et al. (2015) are again plotted in cyan, but only one value of conversion from HCN emission to dense gas mass was used by Liu et al. (2015). Observations of HCN in M51 with a resolution of 1 kpc bridge the gap between the Milky Way clouds and whole galaxies. The green points are based on data in Chen et al. (2015); the higher point is the average for the outer part, while the lower point is for the inner part of M51. A magenta point comes from the study of Milky Way clouds by Heyer et al. (2016) who derived star formation rates from mid-infrared luminosities of Class I protostars in a sample of dense clumps identified in the Atlasgal survey of submillimeter dust emission (Heyer et al. 2016).

Figure 12 shows that the SFE measured for dense gas varies little from local clouds to whole galaxies. These results are very consistent with those found by Liu et al. (2015), but extend them down to the scales of individual clouds in the Galaxy, and even down to the scales of nearby clouds, where the methods of measuring both SFR and M_{dense} are quite different. The basic conclusion is that the mass of dense gas is the most stable predictor of SFE across seven orders of magnitude in dense gas mass. The grand average of the data points in Figure 11 yields $\langle \log \text{SFE}(\text{Myr}^{-1}) \rangle = -2.83 \pm 0.42$ if the (U)LIRGs with the Milky Way value for α_{CO} are included, or -2.73 ± 0.59 if the point using the (U)LIRG value for α_{CO} is included. In contrast, the grand average for the dense gas data in Figure 12 is $\langle \log \text{SFE}(\text{Myr}^{-1}) \rangle = -1.82 \pm 0.19$, with a standard deviation one-third that when all molecular gas is used.

Despite the remarkable consistency shown in Figure 12, M_{dense} , at least as measured by HCN, is not perfect; studies of our Galactic Center and nearby galaxies using HCN $J = 1 \rightarrow 0$ as the tracer of dense gas (Usero et al. 2015; Chen et al. 2015; Longmore et al. 2013) have shown that the SFE for dense gas also depends on environment. This dependence can be seen in Figure 12 where the lowest point is for the inner part of M51. Recent studies show that this decrease in SFE is a function of various galactic properties, such as molecular fraction (Bigiel et al. 2016). The most plausible explanation for lower SFE for gas probed by HCN emission in regions of high density is that the criterion for rapid star formation changes. Kruijssen et al. (2014) provide an exhaustive examination of both global and local mechanisms to explain the low SFE for gas probed by NH_3 emission in the central molecular zone of our Galaxy. They favor episodic star formation among global mechanisms and a much higher threshold density for star formation among local mechanisms. The higher threshold is caused by the greatly increased turbulence in the central molecular zone, pushing the density threshold to values as high as $n \approx 10^7 \text{ cm}^{-3}$, far above the density needed to produce strong emission from HCN $J = 1 \rightarrow 0$ (Evans 1999; Shirley 2015). In these environments, probes of higher densities, such as higher J transitions of HCN, may be more diagnostic of the mass of gas above the threshold density. Further studies of central regions of galaxies, including our own, are needed to refine the criteria for star formation.

There are many reasons why measures of SFE in the range of regions plotted in figures 11 and 12 might differ. The methods used to determine cloud mass and dense gas mass differ and the meaning of “dense” is not the same for all. Extragalactic studies, especially whole galaxy observations, average over a huge range of physical conditions and sample regions at different stages of evolution, while studies of individual clouds are snapshots (Kruijssen & Longmore 2014). The fact that the differences in SFE across this range are so small when measured against dense gas is an important clue for our understanding of what controls star formation. The consistency suggests that simulations of star formation and galaxy evolution that require higher densities to initiate star formation are on the right track. A picture in which most molecular clouds are unbound and only small, dense parts of the clouds are sites of star formation (Dobbs et al. 2011) or a picture in which dense clump formation from more diffuse molecular gas is a continuous process (Burkert & Hartmann 2013) can potentially explain our results. Pictures in which a high density *contrast* is needed for star formation may be able to incorporate the lower SFE for dense gas in galaxy centers (Bigiel et al. 2016). A combination of these ideas may produce a more unified picture. Future work on other galaxies with high spatial resolution, using dense gas tracers, will test these relations further.

8. SUMMARY

We compiled a sample of Galactic MCs that are associated with H II regions and estimated their properties and SFR. The analysis of MCs, H II regions, and SF tracers (both radio continuum and MIR emission) shows different degrees of associations between molecular gas and star formation. We classified the MCs into different groups: MCs with embedded H II regions, MCs with overlapping H II regions, and MCs with separated H II regions. We did not use the last group because association between molecular gas and star formation was too uncertain.

The sample was used to test relations between SFR and properties of MCs. We tested four different models of star formation. No significant correlation was found between ϵ_{ff} and $t_{\text{ff}}/t_{\text{dyn}}$. Significant correlations exist between SFR and M_{cloud} , M_{dense} , and $M_{\text{cloud}}/t_{\text{ff}}$. The relation between SFR and M_{dense} is consistent with linear, while the other two are significantly non-linear, unlike extragalactic relations or the theoretical model by Krumholz et al. (2012) for

$M_{\text{cloud}}/t_{\text{ff}}$.

Combining the data on Galactic Plane clouds presented in this paper with that on nearby clouds shows that the star formation efficiency of the nearby clouds is higher when efficiency is measured versus M_{cloud} or $M_{\text{cloud}}/t_{\text{ff}}$. The efficiency per mass of dense gas is very similar for the nearby clouds and the Galactic plane clouds.

Adding extragalactic studies, we can extend the range of relevant mass scales over 7 orders of magnitude. The star formation efficiency for dense gas shows remarkable stability over this range, varying over a factor of 4, while that for total molecular gas varies by a factor of 40. The standard deviation in the log of the SFE(Myr^{-1}) decreases by about a factor of 3 to a value of 0.19 when dense gas mass, rather than molecular mass, is used.

We thank the anonymous referee for a careful reading and excellent suggestions which have improved the paper. We also thank C. McKee, C. Federrath, G. Parmentier, M. Fall, and B. Ochsendorf for comments. We are grateful to the BGPS team for sharing ideas and information over many years. We particularly thank B. Svoboda for calculations to characterize the extinction threshold for the BGPS sample. H. Chen kindly provided data on galaxies. This work was supported by NSF grant AST-1109116 to the University of Texas at Austin. MH acknowledges support from NASA ADAP grant NNX13AF08G to the University of Massachusetts.

APPENDIX

A. ERROR ANALYSIS

The uncertainties are in general propagated from those arising from the fundamental measurements. Distance errors are not included in the values in the tables such as cloud mass, dense gas mass, and star formation rate because distance cancels out in some quantities, such as star formation efficiency. However, where a star formation rate is plotted versus something like a mass, or where correlation fits are done, a distance error has been incorporated by adding it in quadrature to the uncertainties in SFR or mass. We use sfr and m_{cloud} to represent the SFR and M_{cloud} without the distance factors, so that $\text{SFR} = \text{sfr}D^2$ and $M_{\text{cloud}} = m_{\text{cloud}}D^2$. When $\sigma(\text{sfr})$ or $\sigma(m_{\text{cloud}})$ appear in the equations below, they do not include the distance uncertainties, represented by $\sigma(D)$, but the uncertainty in sfr includes a nominal 10% uncertainty and the cloud mass estimate includes uncertainties from excitation and abundance as follows:

$$\sigma(m_{\text{cloud}}) = m_{\text{cloud}}[(\sigma(N(^{13}\text{CO}))/N(^{13}\text{CO}))^2 + (\sigma(X(^{13}\text{CO}))/X(^{13}\text{CO}))^2]^{0.5}, \quad (\text{A1})$$

where $\sigma(N(^{13}\text{CO}))/N(^{13}\text{CO}) = 0.27$, $\sigma(X(^{13}\text{CO}))/X(^{13}\text{CO}) = 0.30$, and $X(^{13}\text{CO}) = \text{H}_2/^{13}\text{CO}$ (§3.3.1).

For more complex variables, the dependence on distance is based on analysis of how the final quantity depends on the fundamental variables. The quantity $M_{\text{cloud}}/t_{\text{ff}}$ has the following dependency:

$$M_{\text{cloud}}/t_{\text{ff}} \propto M_{\text{cloud}} \times \sqrt{\rho} \propto M_{\text{cloud}} \times \sqrt{\frac{M_{\text{cloud}}}{r_{\text{cloud}}^3}} \propto \frac{M_{\text{cloud}}^{1.5}}{r_{\text{cloud}}^{1.5}} \propto \frac{m_{\text{cloud}}^{1.5} D^{3.0}}{\theta_{\text{cloud}}^{1.5} D^{1.5}} \propto \frac{m_{\text{cloud}}^{1.5} D^{1.5}}{\theta_{\text{cloud}}^{1.5}} \quad (\text{A2})$$

since the uncertainty in cloud size is proportional to distance with fixed angular resolution. Then,

$$\sigma(M_{\text{cloud}}/t_{\text{ff}}) = (M_{\text{cloud}}/t_{\text{ff}})[(1.5\sigma(m_{\text{cloud}})/m_{\text{cloud}})^2 + (1.5\sigma(D)/D)^2]^{0.5} \quad (\text{A3})$$

because uncertainties in θ_{cloud} are negligible compared to those in distance.

Because $\text{SFR} = \text{sfr}D^2$, the efficiency quantity,

$$\epsilon_{\text{ff}} = \text{SFR}/(M_{\text{cloud}}/t_{\text{ff}}) \propto \frac{\text{sfr} D^2}{m_{\text{cloud}}^{1.5} D^{1.5}} \propto \text{sfr} m_{\text{cloud}}^{-1.5} D^{0.5} \quad (\text{A4})$$

and

$$\sigma(\epsilon_{\text{ff}}) = \epsilon_{\text{ff}}[(\sigma(\text{sfr})/\text{sfr})^2 + (0.5\sigma(D)/D)^2 + (1.5\sigma(m_{\text{cloud}})/m_{\text{cloud}})^2]^{0.5} \quad (\text{A5})$$

The quantity $t_{\text{ff}}/t_{\text{dyn}}$ is

$$t_{\text{ff}}/t_{\text{dyn}} = 0.86\sqrt{\alpha} \quad (\text{A6})$$

and

$$\sigma(t_{\text{ff}}/t_{\text{dyn}}) = (t_{\text{ff}}/t_{\text{dyn}})|0.5\sigma(\alpha)/\alpha| \quad (\text{A7})$$

where

$$\sigma(\alpha) = \alpha[(2\sigma(v)/v)^2 + (\sigma(m_{\text{cloud}})/m_{\text{cloud}})^2 + (\sigma(D)/D)^2]^{0.5} \quad (\text{A8})$$

because

$$\alpha = M_{\text{vir}}/M_{\text{cloud}} \propto \frac{\delta v^2 D}{m_{\text{cloud}} D^2} \propto \delta v^2 D^{-1} \quad (\text{A9})$$

REFERENCES

- Aguirre, J. E., Ginsburg, A. G., Dunham, M. K., et al. 2011, *ApJS*, 192, 4
- Anderson, L. D., Bania, T. M., Balsaer, D. S., et al. 2014, *ApJS*, 212, 1
- Anderson, L. D., Bania, T. M., Balsaer, D. S., & Rood, R. T. 2011, *ApJS*, 194, 32
- . 2012, *ApJ*, 754, 62
- Battersby, C., Bally, J., Ginsburg, A., et al. 2011, *A&A*, 535, A128
- Battisti, A. J., & Heyer, M. H. 2014, *ApJ*, 780, 173
- Bigiel, F., Leroy, A., Walter, F., et al. 2008, *AJ*, 136, 2846
- Bigiel, F., Leroy, A. K., Jiménez-Donaire, M. J., et al. 2016, *ApJL*, 822, L26
- Brand, J., & Blitz, L. 1993, *A&A*, 275, 67
- Burkert, A., & Hartmann, L. 2013, *ApJ*, 773, 48
- Calzetti, D., Kennicutt, R. C., Engelbracht, C. W., et al. 2007, *ApJ*, 666, 870
- Chen, H., Gao, Y., Braine, J., & Gu, Q. 2015, *ApJ*, 810, 140
- Chomiuk, L., & Povich, M. S. 2011, *AJ*, 142, 197
- Clemens, D. P. 1985, *ApJ*, 295, 422
- Condon, J. J. 1992, *ARA&A*, 30, 575
- da Silva, R. L., Fumagalli, M., & Krumholz, M. 2012, *ApJ*, 745, 145
- da Silva, R. L., Fumagalli, M., & Krumholz, M. R. 2014, *MNRAS*, 444, 3275
- Dale, J. E., Ngoumou, J., Ercolano, B., & Bonnell, I. A. 2014, *MNRAS*, 442, 694
- Dobbs, C. L., Burkert, A., & Pringle, J. E. 2011, *MNRAS*, 413, 2935
- Dunham, M. K., Rosolowsky, E., Evans, II, N. J., Cyganowski, C., & Urquhart, J. S. 2011, *ApJ*, 741, 110
- Dunham, M. M., Allen, L. E., Evans, II, N. J., et al. 2015, *ApJS*, 220, 11
- Ellsworth-Bowers, T. P., Glenn, J., Riley, A., et al. 2015, *ApJ*, 805, 157
- Evans, II, N. J. 1999, *ARA&A*, 37, 311
- Evans, II, N. J., Heiderman, A., & Vutisalchavakul, N. 2014, *ApJ*, 782, 114
- Evans, II, N. J., Dunham, M. M., Jørgensen, J. K., et al. 2009, *ApJS*, 181, 321
- Fukui, Y., Mizuno, N., Yamaguchi, R., et al. 1999, *PASJ*, 51, 745
- Fumagalli, M., da Silva, R. L., & Krumholz, M. R. 2011, *ApJL*, 741, L26
- Gao, Y., & Solomon, P. M. 2004, *ApJ*, 606, 271
- Ginsburg, A., Glenn, J., Rosolowsky, E., et al. 2013, *ApJS*, 208, 14
- Goldsmith, P. F., Heyer, M., Narayanan, G., et al. 2008, *ApJ*, 680, 428
- Gutermuth, R. A., Pipher, J. L., Megeath, S. T., et al. 2011, *ApJ*, 739, 84
- Hao, C.-N., Kennicutt, R. C., Johnson, B. D., et al. 2011, *ApJ*, 741, 124
- Heiderman, A., Evans, II, N. J., Allen, L. E., Huard, T., & Heyer, M. 2010, *ApJ*, 723, 1019
- Heyer, M., Gutermuth, R., Urquhart, J. S., et al. 2016, *A&A*, 588, A29
- Heyer, M., Krawczyk, C., Duval, J., & Jackson, J. M. 2009, *ApJ*, 699, 1092
- Hildebrand, R. H. 1983, *QJRAS*, 24, 267
- Hughes, A., Meidt, S. E., Colombo, D., et al. 2013, *ApJ*, 779, 46
- Jackson, J. M., Rathborne, J. M., Shah, R. Y., et al. 2006, *ApJS*, 163, 145
- Jacob, J. C., Katz, D. S., Berriman, G. B., et al. 2010, *Montage: An Astronomical Image Mosaicking Toolkit*, Astrophysics Source Code Library, ascl:1010.036
- Kawamura, A., Mizuno, Y., Minamidani, T., et al. 2009, *ApJS*, 184, 1
- Kennicutt, R. C., & Evans, N. J. 2012, *ARA&A*, 50, 531
- Kennicutt, Jr., R. C. 1989, *ApJ*, 344, 685
- . 1998, *ARA&A*, 36, 189
- Kruijssen, J. M. D., & Longmore, S. N. 2014, *MNRAS*, 439, 3239
- Kruijssen, J. M. D., Longmore, S. N., Elmegreen, B. G., et al. 2014, *MNRAS*, 440, 3370
- Krumholz, M. R. 2014, *PhR*, 539, 49
- Krumholz, M. R., Dekel, A., & McKee, C. F. 2012, *ApJ*, 745, 69
- Krumholz, M. R., Fumagalli, M., da Silva, R. L., Rendahl, T., & Parra, J. 2015, *MNRAS*, 452, 1447
- Krumholz, M. R., & McKee, C. F. 2005, *ApJ*, 630, 250
- Lada, C. J., Forbrich, J., Lombardi, M., & Alves, J. F. 2012, *ApJ*, 745, 190
- Lada, C. J., Lada, E. A., Clemens, D. P., & Bally, J. 1994, *ApJ*, 429, 694
- Lada, C. J., Lombardi, M., & Alves, J. F. 2010, *ApJ*, 724, 687
- Lada, C. J., Lombardi, M., Roman-Zuniga, C., Forbrich, J., & Alves, J. F. 2013, *ApJ*, 778, 133
- Leitherer, C., Schaerer, D., Goldader, J. D., et al. 1999, *ApJS*, 123, 3
- Leroy, A. K., Walter, F., Sandstrom, K., et al. 2013, *AJ*, 146, 19
- Liu, L., Gao, Y., & Greve, T. R. 2015, *ApJ*, 805, 31
- Longmore, S. N., Bally, J., Testi, L., et al. 2013, *MNRAS*, 429, 987
- MacLaren, I., Richardson, K. M., & Wolfendale, A. W. 1988, *ApJ*, 333, 821
- Markwardt, C. B. 2009, in *Astronomical Society of the Pacific Conference Series*, Vol. 411, *Astronomical Data Analysis Software and Systems XVIII*, ed. D. A. Bohlender, D. Durand, & P. Dowler, 251
- Matzner, C. D. 2002, *ApJ*, 566, 302
- Miville-Deschênes, M.-A., & Lagache, G. 2005, *ApJS*, 157, 302
- Murray, N. 2011, *ApJ*, 729, 133
- Onodera, S., Kuno, N., Tosaki, T., et al. 2010, *ApJL*, 722, L127
- Ossenkopf, V., & Henning, T. 1994, *A&A*, 291, 943
- Padoan, P., Federrath, C., Chabrier, G., et al. 2014, *Protostars and Planets VI*, 77
- Padoan, P., Haugbølle, T., & Nordlund, Å. 2012, *ApJL*, 759, L27
- Parmentier, G. 2016, *ArXiv e-prints*, arXiv:1605.07623
- Pineda, J. E., Caselli, P., & Goodman, A. A. 2008, *ApJ*, 679, 481
- Pineda, J. L., Goldsmith, P. F., Chapman, N., et al. 2010, *ApJ*, 721, 686
- Reid, M. J., Menten, K. M., Zheng, X. W., et al. 2009, *ApJ*, 700, 137
- Ripple, F., Heyer, M. H., Gutermuth, R., Snell, R. L., & Brunt, C. M. 2013, *MNRAS*, 431, 1296
- Roman-Duval, J., Heyer, M., Brunt, C. M., et al. 2016, *ApJ*, 818, 144
- Roman-Duval, J., Jackson, J. M., Heyer, M., Rathborne, J., & Simon, R. 2010, *ApJ*, 723, 492

- Rosolowsky, E., Keto, E., Matsushita, S., & Willner, S. P. 2007, ApJ, 661, 830
- Rosolowsky, E., & Leroy, A. 2006, PASP, 118, 590
- Rosolowsky, E., Dunham, M. K., Ginsburg, A., et al. 2010, ApJS, 188, 123
- Schlingman, W. M., Shirley, Y. L., Schenk, D. E., et al. 2011, ApJS, 195, 14
- Schmidt, M. 1959, ApJ, 129, 243
- . 1963, ApJ, 137, 758
- Schruba, A., Leroy, A. K., Walter, F., Sandstrom, K., & Rosolowsky, E. 2010, ApJ, 722, 1699
- Schruba, A., Leroy, A. K., Walter, F., et al. 2011, AJ, 142, 37
- Shirley, Y. L. 2015, PASP, 127, 299
- Shirley, Y. L., Ellsworth-Bowers, T. P., Svoboda, B., et al. 2013, ApJS, 209, 2
- Stil, J. M., Taylor, A. R., Dickey, J. M., et al. 2006, AJ, 132, 1158
- Usero, A., Leroy, A. K., Walter, F., et al. 2015, AJ, 150, 115
- Vutisalchavakul, N., & Evans, II, N. J. 2013, ApJ, 765, 129
- Vutisalchavakul, N., Evans, II, N. J., & Battersby, C. 2014, ApJ, 797, 77
- Williams, M. J., Bureau, M., & Cappellari, M. 2010, MNRAS, 409, 1330
- Wright, E. L., Eisenhardt, P. R. M., Mainzer, A. K., et al. 2010, AJ, 140, 1868
- Wu, J., Evans, II, N. J., Gao, Y., et al. 2005, ApJL, 635, L173